Maximizing Independent Channels and Efficiency in BTS Array Antennas via EM Degrees of Freedom

Federico Puggelli, *Member, IEEE*, Bruno Biscontini, *Member, IEEE*, Enrica Martini, *Senior Member, IEEE*, and Stefano Maci, *Fellow, IEEE*

***Abstract*— Massive multiple-input multiple-output (M-MIMO) technology has significantly advanced base station antenna design by integrating many transceivers (TRs) within antenna arrays, thereby improving network capacity and enabling the effective handling of complex multiuser scenario; however, antenna theory and antenna parameters with relevant bounds have not been adapted to this new reality. To address this gap, we propose a theoretical framework aimed at emphasizing the maximum number of independent MIMO channels that an antenna can provide in a cell and compare it with the physical upper bounds, and the latter is provided by the degrees of freedom (DoFs) of the field in the same cell. This approach allows for the definition of novel figures of merit for the quantification of antenna array performance, and the individuation of design strategies targeting the maximization of the number of independent channels, the average efficiency, and the maximum average gain within a specific cell. By exploring the DoF of the electromagnetic (EM) field, we establish the physical upper bounds for system performance. To this end, this article details the embedded element patterns (EEPs), their related efficiency correlation matrix (ECM) and cell correlation matrix (CCM), and orthogonal field modes, discussing the practical implications of these concepts for MIMO systems. The findings underscore the significance of sophisticated antenna models in enhancing network capacity, efficiency, and reliability. This article contributes to the optimization of antenna arrays in the next-generation mobile networks.**

***Index Terms*— Array antennas, array efficiency (AE), correlation matrix, degrees of freedom (DoFs), directivity, realized gain, scattering matrix.**

NOMENCLATURE

MIMO	Multiple-input multiple-output.
DoF	Degree of freedom.
SVD	Singular value decomposition.
BTS	Base transceiver station.
EEP	Embedded element pattern ($\bar{\mathbf{\Psi}}_i(\hat{r})$).
EEE	Embedded element efficiency ($\eta_{i,i}$).
ECM	Efficiency correlation matrix ($\boldsymbol{\eta}$).
CCM	Cell correlation matrix ($\boldsymbol{\eta}^{(c)}$).
$P^{(in)}$ and $P_i^{(in)}$	Array and ith port input power.
$P^{(rad)}$ and $P_i^{(rad)}$	Array and ith port radiated power.
$P^{(rad,c)}$ and $P_i^{(rad,c)}$	Array and port radiated power in a cell.
$\eta_{i,i}^{(c)}$	Efficiency of the ith port in the cell.
$\eta_{i,i}^{(s)}$	Spill-over efficiency of the ith port in the cell.
$\bar{\mathbf{\Phi}}_i(\hat{r})$	Orthonormal field modes (OFMs) radiated by the array.
$\bar{\boldsymbol{\chi}}_i(\hat{r})$	Complete set of OFM radiated by the enveloping surface.
$\bar{\boldsymbol{\eta}}^{(c)}$	CCM associated with $\bar{\boldsymbol{\chi}}_i(\hat{r})$.
$\lambda_i, \lambda_i^{(c)}$, and $\bar{\lambda}_i^{(c)}$	Eigenvalues of $\boldsymbol{\eta}, \boldsymbol{\eta}^{(c)}$, and $\bar{\boldsymbol{\eta}}^{(c)}$, respectively.
N	Number of array ports.
N_{DoF} and $N_{DoF}^{(c)}$	Number of DoF in all space and in the cell, respectively.
N_{MIMO}	Independent MIMO channels in the cell.
$G_i(\hat{r})$	EEP realized gain.
$G_{max}^{(ave)}$	Average maximum realized gain.
$G_{max}^{(ave,c)}$	Average maximum realized gain in the cell.

Received 29 August 2024; revised 1 January 2025; accepted 25 January 2025. Date of publication 7 February 2025; date of current version 4 June 2025. This work was supported by Huawei within the framework of the Huawei–University of Siena Joint Laboratory. The work of Enrica Martini and Stefano Maci was supported in part by the European Union under the Italian National Recovery and Resilience Plan (NRRP) of Next Generation EU, Partnership on "Telecommunications of the Future" through Program "RESTART" under Grant PE00000001. *(Corresponding author: Stefano Maci.)*

Federico Puggelli is with Huawei Technologies Italia Srl, 20147 Milan, Italy (e-mail: federico.puggelli@huawei.com).

Bruno Biscontini is with Huawei Technologies Deutschland, Munich Research Center, 80992 München, Germany (e-mail: Bruno.Biscontini@huawei.com).

Enrica Martini and Stefano Maci are with the Department of Information Engineering and Mathematics, University of Siena, 53100 Siena, Italy (e-mail: martini@dii.unisi.it; macis@dii.unisi.it).

Digital Object Identifier 10.1109/TAP.2025.3537682

I. INTRODUCTION

THIS article presents a theoretical framework to quantify the maximum number of independent MIMO channels that a predefined antenna architecture can establish with multiple users within a communication cell. Additionally, it introduces a straightforward method to determine the physical upper bound of this number using the DoFs of the electromagnetic (EM) field. This work is driven by the increasing demand for basic coverage and high data traffic in mobile communication macro-cellular networks, coupled with the lack of new antenna parameters to more effectively quantify performance limits.

The telecommunication ecosystem, including research and industry, has developed five generations of mobile communication standards and has started working toward the sixth generation (6G). An exhaustive description of these networks can be found in 3rd Generation Partnership Project (3GPP) documents and numerous technical articles [1], [2], [3], [4], [5], [6], [7], [8], [9]. Essentially, three logical building blocks

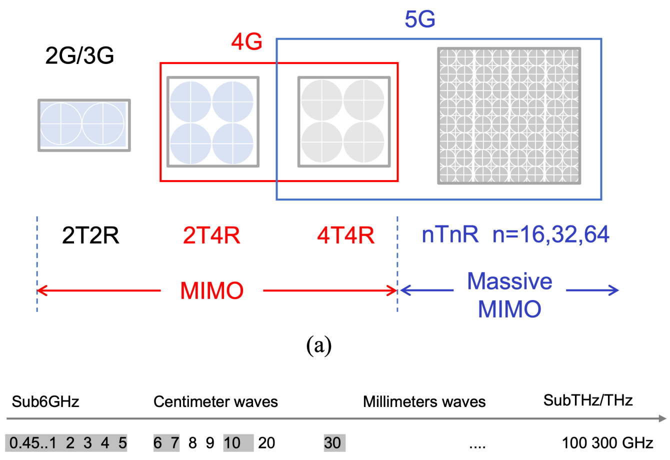

(a)

(b)

Fig. 1. (a) Evolution of antenna array configurations, showcasing different stages from a 2T2R antenna to a highly complex M-MIMO n transmitter n receiver (nTnR) array. (b) Spectrum allocation for mobile communications.

can be identified: the transport network, the radio access network (RAN), and the terminals. Cellular networks are organized in hexagonal-shaped cells, with RAN technology being the most prevalent, as BTS antennas and related equipment can be seen everywhere worldwide.

The foundational architecture of BTS antennas is single arrays or multiple arrays developed according to the standards for spectrum and the number of base station ports. The technology behind BTS antennas is commonly referred to as MIMO or, more recently, massive MIMO (M-MIMO) [8], [9].

Fig. 1(a) shows the evolution of BTS antenna array configurations based on the number of antenna ports paired with transceivers (TRs). The 2G and 3G networks introduced the first attempts at MIMO, in terms of polarization diversity, where two transmitters and two receivers (2T2R) systems were used. Higher order MIMO systems, such as 4T4R, were introduced in 4G, leading in 5G to more sophisticated M-MIMO antennas in which a large number of TR are connected to a large number of antenna ports.

Fig. 1(b) illustrates the frequency bands utilized in mobile communication systems, which must be supported by the BTS antenna systems. The sub-6-GHz frequency spectrum, millimeter waves, and sub-THz/THz bands are utilized in legacy networks, including 5G. Centimeter waves are planned for 6G. A comprehensive description of spectrum allocation can be found in [1], [2], [3], and [4].

MIMO systems enable cellular networks to utilize not only time–frequency signal coding but also the spatial dimension, enhancing channel diversity and capacity. M-MIMO introduces the ability to dynamically handle interference in rich spatial diversity, marking a turning point in base station architectures. To drive numerous antenna ports, integrated TRs with antenna arrays result in systems with only optical and air interfaces (BS-Type 1-O and 2-O) [5], [6].

In this context, antenna arrays play a fundamental role and require advanced modeling to unlock their full potential. Simplified antenna models previously used for performance evaluation are now inadequate [7]. Coupling effects for antenna elements packed within limited space and ultrawideband operation [10], [11], [12], [13], must be addressed. More sophisticated models are, therefore, essential to accurately predict the effects of coupling, interference, and channel distortion, thus enabling the assessment of system performances in dynamic environments.

Antenna arrays, with spatial diversity and advanced beamforming, enable base stations to adapt to dynamic environments. Arrays with a high number of antenna elements, as noted in [14], [15], and [16], optimize spectrum use, reduce interference, and meet bandwidth-intensive demands. M-MIMO enhances spatial DoFs and supports multiple users [17], but challenges such as limited space, coupling, and power consumption complicate densification. Millimeter-wave technologies offer bandwidth benefits but pose propagation and implementation challenges [18]. The transformative impacts of M-MIMO in 5G networks [19] and diversity techniques for reliability [20] are emphasized. Base station arrays are critical to achieving 3GPP New Radio goals [21], while strategies for maximizing 5G network capacity are explored in [22]. Reconfigurable intelligent surfaces (RISs) [23], [24] can redirect fields for enhanced performance but require realistic models to avoid inconsistent predictions. Our framework, with modifications, can establish RIS performance bounds, a topic reserved for a forthcoming article.

In [25] and [26], the concept of observable power in a specific spherical region is introduced as the maximum power that an antenna can receive from a given incident field. The work has been extended in [27] to multiple fields coming from different directions. The selection of independent fields is done in that case by the use of absorbing equivalent Huygens' type currents truncated using optical criteria.

The present analytical framework defines array feeding coefficients linking exact EM field representation to system algorithms, enabling the joint design of antennas and algorithms. Novel performance metrics maximize independent channels, efficiency, and gain. Using DoF theory [28], [29], [30], [31], [32], [33], physical bounds are established by enclosing the array in a virtual surface and defining an arbitrary distribution of equivalent electric and magnetic currents according with the equivalence theorem. The dimension of the radiation operator transforming currents in fields is adopted as a measure of the physical upper bound of the number of MIMO channels of any possible antenna fitting inside the virtual surface. This dimension identifies the DoF and its value is obtained by SVD. This SVD also generates orthogonal modes.

SVD-based modes differ from Harrington's characteristic modes [34] and are further developed in a broader context [35]. Unlike characteristic modes and any other orthogonal mode set, our modes achieve the highest average efficiency, as demonstrated in Appendix A.

Other works enrich MIMO antenna optimization. Spectral efficiency and Q-factor constraints are addressed in [36]. Convex optimization links the Q-factor to capacity, validating characteristic modes for design. Capek and Jelinek [37] focus on efficiency under fixed excitation. Neuman et al. [38] optimize feeding coefficients, balancing efficiency, correlation,

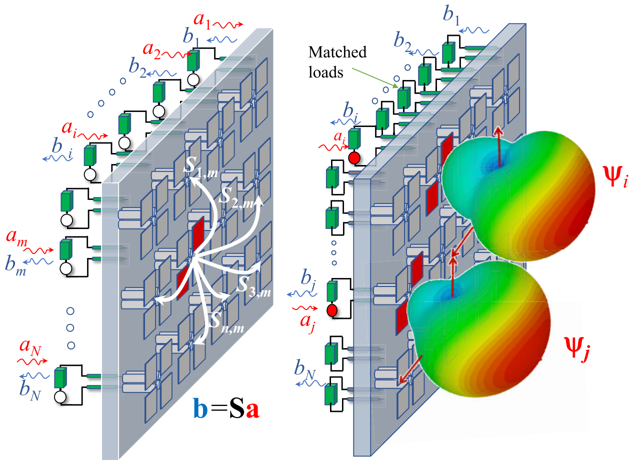

(a) (b)

Fig. 2. (a) Visualization of the incident and reflected waves at the array ports and antenna element interaction through the scattering matrix. (b) EEPs. In the picture, each array element is associated with one port although this is not a restriction.

and power distribution. Mikki [39] explores Shannon limits on EM surface capacity.

This article is structured as follows. Sections II-A–II-D revisit Stein's [40] article, introducing the definition of the EEP and of the ECM including possible losses, and establishing the ECM relationship with the scattering parameter matrix in the absence of losses. Section II-E illustrates the process of orthogonalizing EEPs on an SVD basis. With the help of Appendix A, it demonstrates that this set achieves the maximum average efficiency compared to any other orthogonal set. Section III rigorously proves that the trace of the ECM provides the average maximum antenna gain and underlines the important consequences of it. Section IV introduces the CCM and orthogonal field modes, exploring MIMO channels and gain. Section V analyzes the field radiated by currents on the minimum rectangular surface enclosing the array antenna, defines orthonormal modal currents and fields, and determines the number of DoFs and the complete basis of eigenfields. Building on this, Section VI establishes an upper bound for the number of MIMO-independent channels and for the trace of the CCM, providing theoretical limits for system performance. Section VII presents numerical results relevant to different antenna architectures, illustrating the practical implications of our theoretical findings. Section VIII concludes by summarizing our key insights and their implications for future research and practical applications in the design and optimization of antenna arrays for MIMO systems.

II. EEP and ECM

Throughout this article, vectors are represented using bold characters with a bar on top and matrices with bold characters without bar. Unit vectors will be denoted in bold with a hat.

Consider an antenna array with N ports, as shown in Fig. 2. The array elements are reciprocal but can vary in design or placement, accommodating unconventional configurations. Elements have two polarizations as common in base stations; however, the number of ports will not be necessarily twice the number of elements since subsets of elements are connected through a partial beamforming network (BFN), reducing the number of ports to simplify the system. Ports are indexed from 1 to N, regardless of their association with one or more elements.

The conditions at each antenna port are specified by the complex coefficients of the incident waves a_i and reflected waves b_i, each with units of $\sqrt{W}$. The incident waves are supplied by generators with internal impedance matched to the normalization impedance used in the definition of a_i and b_i. Both the incident and reflected wave coefficients are cast in column vectors $\mathbf{a}$ and $\mathbf{b}$, i.e.,

$$\mathbf{a} = [a_1, a_2, \ldots, a_N]^{\mathrm{T}}$$
$$\mathbf{b} = [b_1, b_2, \ldots, a_N]^{\mathrm{T}}$$

where the superscript T denotes the transposition. The scattering matrix $\mathbf{S}$ at the ports links the complex coefficient vector $\mathbf{b}$ of the reflected wave at the ports with the coefficients of the incident waves $\mathbf{a}$ through $\mathbf{b} = \mathbf{S}\mathbf{a}$ [see Fig. 2(a)]. The entry $S_{i,j}$ of this matrix represents the reflection coefficients at the port i when $i = j$, or the mutual coupling between ports i and j when $i \neq j$.

Here, we use the rms phasors in place of the peak value phasors so that the factors $1/\sqrt{2}$ and $1/2$ are eliminated everywhere in the various equations when representing field and power quantities, respectively.

A. Embedded Element Pattern

One of the key concepts in array theory is the EEP, which refers to the radiation pattern in any direction $\hat{r}$ associated with a specific port within an array when all the other ports are terminated with a matched load [see Fig. 2(b)]. More precisely, the EEP radiation vector $\bar{\boldsymbol{\Psi}}_i(\hat{r})$ of the ith array port is measured or calculated under the following assumptions.

1) The EEP is normalized with respect to the incident power at the ith port, denoted by $P_i^{(in)}$, to simplify the relation with the incident waves used in the definition of the scattering parameters;
2) The remaining ports of the array are terminated with matched loads, so that $a_{j\neq i} = 0$.

Under these conditions, the electric field radiated by the ith array element at a distance r from the origin of the global reference system of the antenna is defined as

$$\bar{\boldsymbol{E}}_i(\bar{r}) = \frac{e^{-jkr}}{r}\sqrt{\zeta_0 P_i^{(in)}}\,\bar{\boldsymbol{\Psi}}_i(\hat{r}) \tag{1}$$

where $\bar{r} = r\hat{\mathbf{r}}$ and ζ_0 is the free-space impedance. With this definition, the EEP is dimensionless, and the relevant *realized gain* $G_i(\hat{r})$ is equal to

$$G_i(\hat{r}) = 4\pi|\bar{\boldsymbol{\Psi}}_i(\hat{r})|^2. \tag{2}$$

It is important to note that, even in the absence of ohmic losses, the directivity of an array element, in general, does not coincide with its gain, as part of the power may be coupled to the other array elements. We note that (2) represents the realized gain, *not* the accepted gain, the latter being normalized with respect to the radiated power plus the power lost for ohmic losses. Conversely, the realized gain also accounts for mismatch and power coupled to other ports.

The effective value of the radiated electric field normalized by $\sqrt{\zeta_0}$ when the array is fed by the incident waves $\{a_i\}$

is given by

$$\frac{\bar{E}(\bar{r})}{\sqrt{\zeta_0}} = \frac{e^{-jkr}}{r}\sum_{i=1}^{N} a_i \bar{\Psi}_i(\hat{r}). \tag{3}$$

B. Efficiency Correlation Matrix

The power radiated by the array is obtained by integrating the flux of Poyinting's vector across a sphere of radius r in the far-field region

$$P^{(rad)} = \frac{1}{\zeta_0}\int\int_{4\pi} |\bar{E}|^2 r^2 d\Omega \tag{4}$$

where $d\Omega = \sin\theta d\theta d\phi$ is the elementary solid angle. Substituting (3) into (4), one has

$$P^{(rad)} = \int\int_{4\pi} \sum_{n,m=1}^{N} a_m^* a_n \bar{\Psi}_m^* \cdot \bar{\Psi}_n d\Omega. \tag{5}$$

It is convenient to define the efficiency correlation matrix (ECM), that is, the Hermitian matrix $\boldsymbol{\eta}$ whose entries are given by

$$\boldsymbol{\eta} = [\eta_{i,j}]_{i,j=1,..N}; \quad \eta_{i,j} = \int\int_{4\pi} \bar{\Psi}_i^* \cdot \bar{\Psi}_j d\Omega. \tag{6}$$

It is worth noting that $\eta_{i,i}$, namely, the ith diagonal entry of the ECM, always positive, represents the EEE of the ith port, $\eta_{EE,i}$, given by the ratio between the power radiated when only the ith port is fed and the incident power at the ith port, i.e.,

$$\eta_{EE,i} = \eta_{i,i}. \tag{7}$$

The total incident and radiated powers for a given set of excitation coefficients $\mathbf{a}$ can be calculated though the following quadratic forms, respectively:

$$P^{(in)} = \mathbf{a}^{\mathrm{H}}\mathbf{a} \tag{8}$$

$$P^{(rad)} = \mathbf{a}^{\mathrm{H}}\boldsymbol{\eta}\mathbf{a} \tag{9}$$

where the superscript H denotes the conjugate transpose.

C. Link Between Lossless ECM and Scattering Matrix

In the absence of ohmic losses, the radiated power is given by

$$|\mathbf{a}|^2 - |\mathbf{b}|^2 = \mathbf{a}^{\mathrm{H}}(\mathbf{1} - \mathbf{S}^{\mathrm{H}}\mathbf{S})\mathbf{a} = \mathbf{a}^{\mathrm{H}}\boldsymbol{\eta}\mathbf{a} \tag{10}$$

where $\mathbf{1}$ is the identity matrix. Note that the factor 1/2 is not present in the first term in (10) since we are considering effective values of incident and reflected waves. The last two members of (10) are quadratic forms associated with Hermitian matrices. In such a case, the equality of the quadratic forms implies the equality of the Hermitian matrices. Therefore, we conclude that [40], [41]

$$\mathbf{1} - \mathbf{S}^{\mathrm{H}}\mathbf{S} = \boldsymbol{\eta}. \tag{11}$$

We emphasize that this is valid only in the absence of losses. From (11), one can see that $\mathbf{S} \to \mathbf{0}$, and $\boldsymbol{\eta} \to \mathbf{1}$ in the limit of vanishing coupling and matched ports. Written entry by entry, (11) reads

$$\eta_{i,j} = -\sum_{n=1}^{N} s_{n,i}^* s_{n,j} \qquad \text{for} \quad i \neq j \tag{12}$$

$$\eta_{EE,i} = 1 - \sum_{n=1}^{N} |s_{i,n}|^2 \tag{13}$$

where we have made use of (7) and of the symmetry of the scattering matrix. It is important to observe that, in the presence of losses, the last equality in (10) is no longer valid, as the incident power minus the reflected power at the ports is larger than the radiated power, i.e., $\mathbf{a}^{\mathrm{H}}(\mathbf{1} - \mathbf{S}^{\mathrm{H}}\mathbf{S})\mathbf{a} > \mathbf{a}^{\mathrm{H}}\boldsymbol{\eta}\mathbf{a}$.

We also observe that (11) indicates that the correlation matrix depends on the near-field interactions among the elements, despite being defined solely in terms of the far field. This is because the EEP inherently depends on these interactions. For a planar periodic array, the aperture field that generates the EEP differs significantly from that of the isolated element and is highly dependent on the interelement spacing.

D. Maximum AE

By using (8) and (9), the array efficiency (AE) for a given set of incident wave coefficients $\mathbf{a}$ is expressed as

$$\eta_{\mathbf{a}} = \frac{P^{(rad)}}{P^{(in)}} = \frac{\mathbf{a}^{\mathrm{H}}\boldsymbol{\eta}\mathbf{a}}{\mathbf{a}^{\mathrm{H}}\mathbf{a}}. \tag{14}$$

In the absence of ohmic losses, (11) implies

$$\eta_{\mathbf{a}} = 1 - \frac{\mathbf{a}^{\mathrm{H}}(\mathbf{S}^{\mathrm{H}}\mathbf{S})\mathbf{a}}{\mathbf{a}^{\mathrm{H}}\mathbf{a}}. \tag{15}$$

Equation (14) identifies the AE as the Rayleigh quotient of the ECM. This implies that the AE ranges between the minimum eigenvalue λ_{min} and the maximum eigenvalue λ_{max} of $\boldsymbol{\eta}$, i.e.,

$$\lambda_{min} \leq \eta_{\mathbf{a}} \leq \lambda_{max}. \tag{16}$$

In the case of completely decoupled and matched ports, the ECM coincides with the identity matrix, and both the maximum and the minimum eigenvalues are equal to 1. Therefore, any excitation gives a maximum, unitary efficiency.

E. Orthogonal Set of EEPs

Since $\boldsymbol{\eta}$ is Hermitian, it can be diagonalized by means of a unitary matrix $\mathbf{Q}$, namely,

$$\boldsymbol{\eta} = \mathbf{Q}\Lambda\mathbf{Q}^{\mathrm{H}} \tag{17}$$

where Λ is a diagonal matrix with the eigenvalues λ_i of $\boldsymbol{\eta}$ on the diagonal. It is not restrictive to assume that these eigenvalues are arranged in decreasing order; this corresponds to an SVD-type diagonalization. In the absence of losses, (11) implies that $\mathbf{Q}$ also diagonalizes $\mathbf{S}^{\mathrm{H}}\mathbf{S}$ with $1 - \lambda_j$ as eigenvalues.

Using (17) and the unitary property of $\mathbf{Q}$, one has

$$\eta_{\mathbf{a}} = \frac{\mathbf{a}^{\mathrm{H}}\mathbf{Q}\Lambda\mathbf{Q}^{\mathrm{H}}\mathbf{a}}{\mathbf{a}^{\mathrm{H}}\mathbf{Q}\mathbf{Q}^{\mathrm{H}}\mathbf{a}}. \tag{18}$$

The above quantity can also be seen as the efficiency of an array with a diagonal correlation matrix Λ (corresponding to *orthonormal* EEPs), fed by a set of incident wave coefficients $\mathbf{a}' = \mathbf{Q}^{\mathrm{H}}\mathbf{a}$ (equivalent to $\mathbf{a} = \mathbf{Q}\mathbf{a}'$), i.e.,

$$\eta_{\mathbf{a}'} = \frac{\mathbf{a}'^{\mathrm{H}}\Lambda\mathbf{a}'}{\mathbf{a}'^{\mathrm{H}}\mathbf{a}'}. \tag{19}$$

Since $\mathbf{a}'$ is arbitrary, we can consider the N elements of the canonical basis $\mathbf{a}' = \mathbf{a}'_j = [0, \ldots, a'_j = 1, \ldots, 0]^{\mathrm{T}}$, which correspond to $\mathbf{a} = \mathbf{q}^{(j)}$, where $\mathbf{q}^{(j)}$ is the jth column of $\mathbf{Q}$.

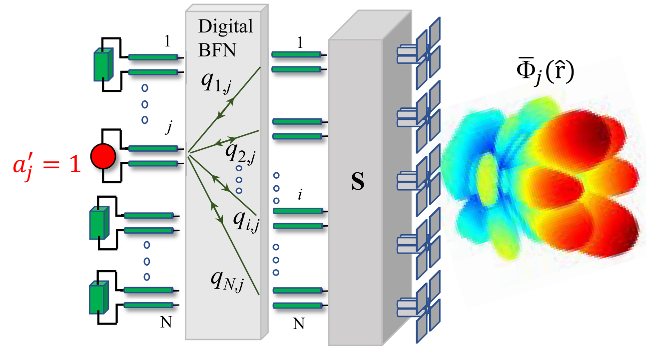

Fig. 3. Symbolic representation of a digital BFN for obtaining orthogonal EEP based on the SVD decomposition of the ECM (transmission scheme). Each mode has an efficiency that is the ith eigenvalues λ_i of the matrix $\mathbf{Q}$.

The set of EEPs

$$\bar{\Phi}_j(\hat{r})) = \sum_{i=1}^{N} q_{i,j}\bar{\Psi}_i(\hat{r}) \tag{20}$$

for $j = 1, \ldots, N$ are, therefore, orthogonal. The jth radiation pattern obtained with this excitation exhibits radiation efficiency equal to λ_j since the ECM of this set of EEPs is Λ.

A digital BFN with N ports $j = 1, \ldots, N$ in input and N ports $i = 1, \ldots, N$ in output, with output ports connected to the N input ports of the array, may be implemented to construct this orthogonal mode set. This BFN, symbolically represented in Fig. 3, has the same complexity as an M-MIMO digital BFN.

In Appendix A, it is shown that the SVD-based modes defined in (20) are characterized by the largest average efficiency among all the sets of excitations resulting in orthogonal radiated far fields.

Before proceeding further, we should note that signals can be distinguished at the user level using pilot signals transmitted as part of the communication protocol. Each user, knowing their specific pilot code, decodes their intended signal by correlating the received signal with the pilot, effectively separating it from others in a multiuser scenario.

III. Effective Number of Ports and Average Maximum Realized Gain

Generally, the efficiency of an array depends on the set of excitation coefficients. It is beneficial to establish an efficiency figure of merit independent of the excitation and solely determined by the ECM.

A. Effective Number of Ports

An invariant parameter of the ECM is its trace, i.e., the sum of its eigenvalues, given by

$$\mathrm{trace}(\boldsymbol{\eta}) = \sum_{i=1}^{N} \eta_{EE,i} = \sum_{i=1}^{N} \lambda_i. \tag{21}$$

In the absence of losses, this trace can also be related through (13) to the sum of the squared amplitudes of the scattering parameters through

$$\mathrm{trace}(\boldsymbol{\eta}) = N - \sum_{i,j=1}^{N} |s_{i,j}|^2 = N - ||\mathbf{S}||^2 \tag{22}$$

where $||(.)||$ denotes the Frobenius norm. This shows that in the absence of port coupling and mismatch, the trace of the ECM coincides with the number of ports. The trace of the ECM can be, therefore, interpreted as an *effective number of ports*. In large arrays with a regular lattice and one port per element, it is often assumed that the interactions among the elements are similar to those in an infinite array. This leads to the approximation $\mathrm{trace}(\boldsymbol{\eta}) \approx 2\pi/\lambda^2$, as shown in Appendix B.

B. Average Maximum Realized Gain

Given a certain set of coefficients $\mathbf{a}$, the realized gain of the array in direction $\hat{r}$ and along a general complex polarization unit vector $\hat{p}$ is given by

$$G(\hat{r}, \hat{p}) = 4\pi \frac{\mathbf{a}^{\mathrm{H}}\mathbf{u}\mathbf{u}^{\mathrm{H}}\mathbf{a}}{\mathbf{a}^{\mathrm{H}}\mathbf{a}} \tag{23}$$

where $\mathbf{u}$ is a column vector with entry $u_n = \bar{\Psi}_n(\hat{\mathbf{r}}) \cdot \hat{p}^*$. The Rayleigh quotient in (23) of the matrix $\mathbf{U} = \mathbf{u}\mathbf{u}^{\mathrm{H}}$ is maximized for $\mathbf{a} = \mathbf{u}$, and the value of the maximum gain along the polarization $\hat{p}$ is

$$G_{max}(\hat{r}, \hat{p}) = 4\pi\mathbf{u}^{\mathrm{H}}\mathbf{u}. \tag{24}$$

Repeating the same procedure for the maximum realized gain associated with the polarization unit vector $\hat{r} \times \hat{p}^*$, one obtains $G_{max}(\hat{r}, \hat{r} \times \hat{p}^*) = 4\pi\mathbf{v}^{\mathrm{H}}\mathbf{v}$ where $\mathbf{v}$ is a column vector with entries $v_n = \bar{\Psi}_n \cdot \hat{r} \times \hat{p}$. The sum of the maximum gain associated with two orthogonal polarizations, i.e.,

$$G_{max}^{(\Sigma)}(\hat{r}) = G_{max}(\hat{r}, \hat{p}) + G_{max}(\hat{r}, \hat{r} \times \hat{p}^*) \tag{25}$$

can be written as

$$\begin{aligned} G_{max}^{(\Sigma)}(\hat{r}) &= 4\pi\left(\mathbf{u}^{\mathrm{H}}\mathbf{u} + \mathbf{v}^{\mathrm{H}}\mathbf{v}\right) = 4\pi \sum_{n=1}^{N} |\bar{\Psi}_n(\hat{\mathbf{r}})|^2 \\ &= \sum_{n=1}^{N} G_n(\hat{r}) \end{aligned} \tag{26}$$

where the last equality comes from (2). We note that this result is independent by $\hat{p}$. This means that the sum of the maximum realized gain for two orthogonal polarizations in any spatial direction is the sum of the individual EEPs realized gains in the same direction. Comparing (26) with (6) leads to a direct link between the trace of $\boldsymbol{\eta}$ and the average maximum gain among all the directions of observation, i.e.,

$$G_{max}^{(ave)} = \frac{1}{4\pi} \int\int_{4\pi} G_{max}^{(\Sigma)}(\hat{r})d\Omega = \mathrm{trace}(\boldsymbol{\eta}). \tag{27}$$

The exact equality described above can be summarized by stating that *the effective number of ports is equal to the sum of the average maximum realized gain for the two polarizations*. If the EEPs are completely uncorrelated and the conditions of perfect matching and the absence of losses are verified, the realized gain coincides with the directivity, and its average maximum value matches the number of antenna elements in the array, N. Therefore, (27) constitutes a generalization to the realized gain of the result presented in [42] for the directivity.

IV. Maximization of Power Inside a Cell

In communication systems, it is important not only to maximize the overall AE, but also mainly to maximize the AE inside a certain subspace of the uv plane, identified as "cell" in wireless terminology. In such a case, it is important to characterize the antenna in terms of power radiated *inside the cell* versus the total radiated power. The power radiated inside the cell is calculated as in (5) except that the integration is performed only over the cell region, i.e.,

$$P^{(rad,c)} = \int\int_{\Omega_C} \sum_{n,m=1}^{N} a_m^* a_n \bar{\Psi}_m^* \cdot \bar{\Psi}_n d\Omega \tag{28}$$

where Ω_C is the solid angle that frames the cell.

A. Cell Correlation Matrix

It is convenient to introduce a modified version of the ECM, denoted here as CCM, in which the far-field integration of the correlation entries is performed only inside the cell. This CCM, denoted as $\boldsymbol{\eta}^{(c)}$, is still a Hermitian matrix whose entries are defined as

$$\eta_{i,j}^{(c)} = \int\int_{\Omega_C} \bar{\Psi}_i^* \cdot \bar{\Psi}_j d\Omega. \tag{29}$$

We note that the normalization of the EEPs in (29) is always based on the input power at each port; only the integration process is defined on a different domain. Therefore, the diagonal entries $\eta_{i,i}^{(c)}$ of $\boldsymbol{\eta}^{(c)}$ represent the efficiency of the EEP with respect to the cell, namely,

$$\eta_{i,i}^{(c)} = P_i^{(rad,c)} / P_i^{(in)}. \tag{30}$$

To better interpret these entries, it is convenient to multiply and divide $\eta_{i,i}^{(c)}$ by $P_i^{(rad)}$, thus obtaining

$$\eta_{i,i}^{(c)} = \eta_{i,i}^{(s)} \eta_{i,i} \tag{31}$$

where $\eta_{i,i}^{(s)} = \eta_{i,i}^{(c)} / \eta_{i,i} = P_i^{(rad,c)} / P_i^{(rad)}$ is the "spill-over" efficiency of the EEP, which is the ratio between the power radiated by the port i in the cell and the power radiated by the same port everywhere in space.

The integral in (28) can be written as

$$P^{(rad,c)} = \mathbf{a}^{\mathrm{H}} \boldsymbol{\eta}^{(c)} \mathbf{a}. \tag{32}$$

The efficiency $\eta_{\mathbf{a}}^{(c)}$ of the array in serving the cell (cell AE) for a set of input coefficients $\mathbf{a}$ is, therefore, defined as the ratio between the power radiated inside the cell and the input power

$$\eta_{\mathbf{a}}^{(c)} = \frac{\mathbf{a}^{\mathrm{H}} \boldsymbol{\eta}^{(c)} \mathbf{a}}{\mathbf{a}^{\mathrm{H}} \mathbf{a}}. \tag{33}$$

We observe that (33) is the Rayleigh quotient of the Hermitian matrix $\boldsymbol{\eta}^{(c)}$. This allows the series of results derived in Sections II and III for $\boldsymbol{\eta}$ to be applied also to $\boldsymbol{\eta}^{(c)}$. Specifically, the maximum cell efficiency is bounded by the maximum eigenvalue of $\boldsymbol{\eta}^{(c)}$.

B. Orthogonal Field Modes in the Cell

The SVD applied to $\boldsymbol{\eta}^{(c)}$, namely,

$$\boldsymbol{\eta}^{(c)} = \mathbf{Q}^{(\mathbf{c})} \Lambda^{(\mathbf{c})} \mathbf{Q}^{(\mathbf{c})\mathrm{H}} \tag{34}$$

provides the unitary matrix $\mathbf{Q}^{(c)}$ whose columns represent the optimal set of incident wave coefficients for achieving maximum average efficiency inside the cell. These coefficients are associated with orthogonal fields inside the cell.

C. Independent Number of MIMO Channels

The number N_{MIMO} of independent MIMO channels is given by the number of significant eigenvalues of the correlation matrix $\boldsymbol{\eta}^{(c)}$, i.e., by the effective rank of $\boldsymbol{\eta}^{(c)}$. We note that, if the CCM is not full rank, some of its eigenvalues may fall below an acceptable threshold. This indicates that the effective number of channels is determined by the number of singular values exceeding the specified threshold, representing the effective rank of the CCM. The definition of this effective rank relies on the chosen threshold. An accredited, self-consistent approach uses the formula proposed in [43], [44]

$$N_{MIMO} \approx \mathrm{rank}_e\left(\boldsymbol{\eta}^{(c)}\right) = \mathrm{round}\frac{\left[\mathrm{trace}\left(\boldsymbol{\eta}^{(c)}\right)\right]^2}{||\boldsymbol{\eta}^{(c)}||^2}$$
$$= \mathrm{round}\frac{\left(\sum_i \lambda_i^{(c)}\right)^2}{\sum_i \left(\lambda_i^{(c)}\right)^2} \leq N \tag{35}$$

where $||(.)||$ is the Frobenius norm and $\mathrm{round}(x)$ is the integer number closest to x. Furthermore, $\mathrm{trace}(\boldsymbol{\eta}^{(c)})$ can be interpreted as an "effective number of channels," where differently from $\mathrm{trace}(\boldsymbol{\eta})$, the efficiency takes into account not only the power lost for mismatch and coupling to other ports, but also the power radiated outside the cell. We also note that $\mathrm{trace}(\boldsymbol{\eta}^{(c)}) < \mathrm{rank}_e(\boldsymbol{\eta}^{(c)})$ since all the eigenvalues of $\boldsymbol{\eta}^{(c)}$) are less than 1. It is worth noting that an extreme densification of ports, in general, does not imply an increased number of independent channels. Additionally, when observing within a cell, it may not always be necessary to connect each element of the array to an individual port. To reduce complexity, it might be more convenient to group some elements of the array together, while still exploiting the DoF of the cell. This concept will be further emphasized in Section V.

D. Average Maximum Realized Gain in the Cell

Equation (33) enables a generalization of (27) to the average maximum gain inside the cell, i.e.,

$$\frac{\Omega_c}{4\pi} G_{max}^{(ave,c)} = \mathrm{trace}\left(\boldsymbol{\eta}^{(c)}\right) \tag{36}$$

where

$$G_{max}^{(ave,c)} = \frac{1}{\Omega_c} \int\int_{\Omega_c} G_{max}^{(\Sigma)}\left(\hat{r}\right) \sin\theta d\theta d\phi \tag{37}$$

where we stress that the superscript Σ in the integrand indicates that one should sum the maximum gain for the two polarizations. This formula substantiates the importance of the trace of the CCM to identify the performance of antennas and allows for the definition of a new parameter, the *average maximum gain efficiency of the antenna* [see (72)].

V. DoFs of the EM Field and Complete Set of Orthogonal Modes

In the previous section, we have identified N_{MIMO} as the maximum number of independent channels that a given base

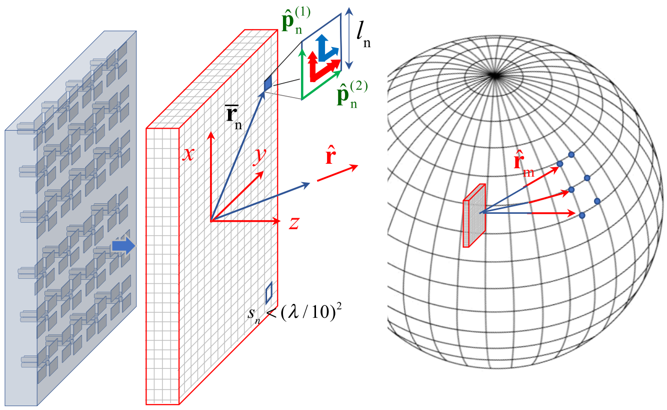

(a) (b)

Fig. 4. (a) Box enveloping the array and relevant meshing for defining electric and magnetic basis functions. (b) Far-field lattice and sampling of directions $\hat{\boldsymbol{r}}_m \equiv (\theta_m, \phi_m)$ for the definition of a complete set of orthogonal modes.

station antenna can establish with multiple users arbitrarily located in a certain cell. In this section, we will link this number with the number of DoFs of the field, N_{DoF} [28], [29], [31], [32], [45]. The latter is not referred to base station and users, but to a generic source distribution inside a region of space and to the EM field observed in another region. In particular, N_{DoF} is defined as the minimum number of independent scalar parameters sufficient to define any field radiated in a certain space region by a confined source. This number actually depends on the source and the observation region size. In this section, we will consider first the whole space as observation domain, to identify a complete basis of orthogonal modes over the entire space. In the next section, it will be shown that N_{DoF} constitutes the upper bound of N_{MIMO} for any possible MIMO antenna serving a certain cell.

A. Field Radiated by Generic Currents Distributed on a Minimum Rectangular Surface Surrounding the Array Antenna

A generic array antenna can be enclosed by a minimal surface, typically modeled as a rectangular box, as shown in Fig. 4. According to the equivalence theorem, any potential source within the box can be represented by a distribution of electric and magnetic currents on its surface. For the sake of simplicity, we will use rectangular subdomains with dimensions that are small compared to the wavelength (e.g., $\lambda/10$), and with currents assumed to be uniform within each subdomain. Therefore, the surface of the box is partitioned using a mesh with N_b square facets, with $N_b \gg N$. At the center of the generic nth facet, a pair of orthogonal basis functions is defined

$$\bar{\boldsymbol{l}}_n^{(i)} = l_n \eta_n \hat{\boldsymbol{p}}_n^{(i)} \tag{38}$$

with $i = 1, 2$, $l_n = \sqrt{s_n}$, where s_n is the area of facet, η_n is a rectangular function which is 1 on the facet and zero elsewhere, and $\hat{\boldsymbol{p}}_n^{(1,2)}$ are the orthogonal unit vectors tangent to the facet. It should be noted that $\bar{\boldsymbol{l}}_n^{(i)} \cdot \bar{\boldsymbol{l}}_m^{(j)} = s_n \delta_{i,j} \delta_{n,m}$, where $\delta_{i,j}$ and $\delta_{n,m}$ are the Kronecker delta functions.

Any arbitrary electric and magnetic currents $\boldsymbol{J}$ and $\boldsymbol{M}$ can be expanded in terms of the defined basis functions as

$$\bar{\boldsymbol{J}} = \sum_{n=1}^{N_b} \sum_{i=1}^{2} J_n^{(i)} \bar{\boldsymbol{l}}_n^{(i)} \qquad \bar{\boldsymbol{M}} = \zeta_0 \sum_{n=1}^{N_b} \sum_{i=1}^{2} \tilde{J}_n^{(i)} \bar{\boldsymbol{l}}_n^{(j)}. \tag{39}$$

The dimensions of $J_n^{(i)}$ and $\tilde{J}_n^{(i)}$ are both A/m. We note that (38) identifies the right-hand side of (39) as a summation of dipolar current moments. We also note that even if $\tilde{J}_n^{(i)}$ has the dimension of a surface *electric* current, the right-hand side of the second equation in (39) represents a sum of normalized surface *magnetic* current moments, thanks to the normalization by the free-space impedance ζ_0. This is a usual approach in all method of moments problems involving interacting electric and magnetic currents in order to avoid ill-conditioning [46]. It should be noted that we do not assume specific impedance boundary conditions on any portion of the surface (e.g., we do not eliminate a priori electric currents on that portion of the box surface where a perfectly electric ground plane is located).

The DoF number N_{DoF} is given by the dimension of the radiation operator that transforms the currents over the box into the field in the observation region. Although the process can be applied for an arbitrary observation region, even in the Fresnel zone, we will apply here the radiation operator in the far zone. To this end, we define an angular lattice uniform in θ and ϕ, with sampling intervals $\Delta\theta$ and $\Delta\phi$, and sampling direction unit vectors $\hat{\boldsymbol{r}}_m \equiv (\theta_m, \phi_m)$ with $m = 1, \ldots, M$. As for previous quantities, we will treat effective values of field and currents, so that we will omit the factor 2 at the denominator in the power expressions. The electric field radiated in the far zone, normalized by $\sqrt{\zeta_0}$, is given by

$$\frac{\bar{E}_m}{\sqrt{\zeta_0}} = \frac{e^{-jkr}}{r} \sum_{i=1}^{2} \sum_{n=1}^{N_b} l_n \left(\bar{A}_n^{(i)}(\hat{\boldsymbol{r}}_m) J_n^{(i)} + \bar{B}_n^{(i)}(\hat{\boldsymbol{r}}_m) \tilde{J}_n^{(i)} \right) \tag{40}$$

where

$$\bar{A}_n^{(i)}(\hat{\mathbf{r}}) = e^{jk\hat{r}\cdot\bar{r}_n} \frac{jk\sqrt{\zeta_0}}{4\pi} \hat{\boldsymbol{r}} \times \hat{\boldsymbol{r}} \times \boldsymbol{l}_n^{(i)} \sqrt{\sin\theta \Delta\theta \Delta\phi} \tag{41}$$

$$\bar{B}_n^{(i)}(\hat{\mathbf{r}}) = e^{jk\hat{r}\cdot\bar{r}_n} \frac{jk\sqrt{\zeta_0}}{4\pi} \hat{\boldsymbol{r}} \times \boldsymbol{l}_n^{(i)} \sqrt{\sin\theta \Delta\theta \Delta\phi} \tag{42}$$

and $\bar{\boldsymbol{r}}_n$ is the position vector of the center of the nth facet. The previous equation can be cast into a $2M \times 2N_b$ linear system with matrix form

$$\mathbf{V} = \mathbf{F}\mathbf{I} \tag{43}$$

where

$$\mathbf{V} = re^{(jkr)} \sqrt{\zeta_0} \left[\mathbf{E}_m \cdot \hat{\theta}_m, \mathbf{E}_m \cdot \hat{\phi}_m \right]^{\mathrm{T}} \tag{44}$$

$$\mathbf{I} = \left[J_n^{(1)} l_n, J_n^{(2)} l_n, \tilde{J}_n^{(1)} l_n, \tilde{J}_n^{(2)} l_n \right]^{\mathrm{T}} \tag{45}$$

$$\mathbf{F} = \begin{bmatrix} \bar{A}_{mn}^{(1)} \cdot \hat{\theta}_m & \bar{A}_{mn}^{(2)} \cdot \hat{\theta}_m & \bar{B}_{mn}^{(1)} \cdot \hat{\theta}_m & \bar{B}_{mn}^{(2)} \cdot \hat{\theta}_m \\ \bar{A}_{mn}^{(1)} \cdot \hat{\phi}_m & \bar{A}_{mn}^{(2)} \cdot \hat{\phi}_m & \bar{B}_{mn}^{(1)} \cdot \hat{\phi}_m & \bar{B}_{mn}^{(2)} \cdot \hat{\phi}_m \end{bmatrix} \tag{46}$$

where $\bar{A}_{nm}^{(i)} = \bar{A}_n^{(i)}(\hat{\mathbf{r}}_m)$ and $\bar{B}_{nm}^{(i)} = \bar{B}_n^{(i)}(\hat{\mathbf{r}}_m)$.

We note that the dimensions of $[\mathbf{V}]$, $[\mathbf{F}]$, and $[\mathbf{I}]$ are $[\mathrm{W}]^{1/2}$, $[\Omega]^{1/2}$, and [A], respectively. The various quantities are normalized in such a way that the radiated power, defined by the integral of the power density all over the space, is given by $||\mathbf{V}||^2$ in the limit of vanishing angular intervals. We will define a reference current $|I_0|$ as the mean square of the electric current density plus the normalized magnetic current density over the box surface, namely,

$$|I_0|^2 = \frac{1}{s}\int\int_s\left(|\mathbf{J}|^2 + \frac{1}{\zeta_0^2}|\mathbf{M}^2|\right)ds \tag{47}$$

where s is the surface of the box. Under this assumption, one has

$$|I_0|^2 = \frac{1}{s}\sum_1^{N_b} s_n\left(\sum_{i=1}^{2}|J_n^{(i)}|^2 + |\tilde{J}_n^{(i)}|^2\right) = ||\mathbf{I}||^2. \tag{48}$$

This implies a definition of the radiation resistance of the current distribution as the Rayleigh quotient of the matrix $\mathbf{F}^{\mathrm{H}}\mathbf{F}$

$$R_{rad} = \frac{P^{(rad)}}{|I_0|^2} = \frac{||\mathbf{V}||^2}{||\mathbf{I}||^2} = \frac{\mathbf{I}^{\mathrm{H}}\mathbf{F}^{\mathrm{H}}\mathbf{F}\ \mathbf{I}}{\mathbf{I}^{\mathrm{H}}\mathbf{I}}. \tag{49}$$

Hence, the maximum radiation resistance is given by the maximum eigenvalue of the matrix $\mathbf{F}^{\mathrm{H}}\mathbf{F}$.

B. Orthonormal Modal Currents and Fields

The matrix $\mathbf{F}$ can be factorized via SVD into

$$\mathbf{F} = \mathbf{v}\Sigma\mathbf{i}^{\mathrm{H}} \tag{50}$$

where $\mathbf{v}$ and $\mathbf{i}$ are the unitary dimensionless matrices, i.e., $\mathbf{v}^{\mathrm{H}}\mathbf{v} = \mathbf{1}_M$ and $\mathbf{i}^{\mathrm{H}}\mathbf{i} = \mathbf{1}_{N_b}$. Furthermore, $\Sigma = diag(\sigma_1, \sigma_2 \ldots)$ is a diagonal $M \times N_b$ matrix containing the singular values σ_i, with dimensions of [Omega]$^{1/2}$, arranged in descending order.

Let us consider the jth column $\mathbf{v}_j$ of $\mathbf{v}$ and the jth column $\mathbf{i}_j$ of $\mathbf{I}$. From (50), one has

$$\mathbf{F}\mathbf{i}_j = \mathbf{v}_j\sigma_j \tag{51}$$

where $||\mathbf{v}_j|| = 1$ and $||\mathbf{i}_j|| = 1$ since both $\mathbf{v}$ and $\mathbf{i}$ are unitary matrices. Equation (51), therefore, defines a set of orthogonal and unitary modal current distributions whose coefficients are given by the entries of the vector $\mathbf{i}_j$. The jth modal current radiates a field whose samples in the far zone are given by the entries of $\mathbf{v}_j\sigma_j$. The radiated power associated with the jth modal current, obtained by integrating the normalized far field over the full space, is therefore, identified with the squared norm of this radiated field and is given by $||\mathbf{v}_j||^2\sigma_j^2 = \sigma_j^2$. In summary, the matrix $\mathbf{F}$ is normalized in such a way that each jth current mode coming from its SVD radiates in all the space a power equal to σ_j^2; therefore, σ_j^2 represents the radiation resistance $R_{rad,j}$ of the modal currents, i.e.,

$$R_{rad,j} = \sigma_j^2. \tag{52}$$

It is also worth noting that the square of the singular values of $\mathbf{F}$ corresponds to the real positive eigenvalues ξ_j of $\mathbf{F}^{\mathrm{H}}\mathbf{F}$ ordered in descending values. Therefore, from (52), the maximum radiation resistance is given by

$$R_{rad}^{max} = \sigma_{max}^2 = \xi_{max}. \tag{53}$$

C. Number of DoFs in All Space

In sampling the distribution of currents and fields, one should take care about having a significant redundancy with respect to a half-wavelength sampling. This implies that there is a tale of singular values with very small values. The number N_{DoF} of DoFs of the far field radiated by the currents on the box is the effective rank of $\mathbf{F}^{\mathrm{H}}\mathbf{F}$, that is, the number of its significant singular values. This latter can be calculated by using a modification of the formula proposed in [43], [44]

$$N_{DoF} = \mathrm{rank}_e\left(\mathbf{F}^{\mathrm{H}}\mathbf{F}\right) = 2\,\mathrm{ceil}\left\{\frac{\xi}{2} + \sqrt{2\xi}\right\} \tag{54}$$

$$\xi = \frac{\mathrm{trace}\left\{\left(\mathbf{F}^{\mathrm{H}}\mathbf{F}\right)\right\}^2}{||\mathbf{F}^{\mathrm{H}}\mathbf{F}||^2} = \frac{\left(\sum_i \sigma_i^2\right)^2}{\sum_i \sigma_i^4} \tag{55}$$

where ceil$\{x\}$ represents the smallest integer greater than or equal to the argument x and rank$_e$ denotes the effective rank. The above way to count the significant number of singular values is self-consistent, that is, it does not need to define a threshold. We note that we have included a certain redundancy with respect to the criterion defined in (35). This is done in order to ensure the completeness of the eigenfield basis defined in the following section.

D. Relation Between Trace and Average Maximum Directivity

Using the same derivation as the one in Section III-B, it can be shown that

$$D_{max}^{(ave)} = \frac{1}{4\pi}\int\int_{4\pi} D_{max}^{(\Sigma)}(\hat{r})d\Omega = \mathrm{trace}\left(\mathbf{F}^{\mathrm{H}}\mathbf{F}\right) \tag{56}$$

where $D_{max}^{(\Sigma)}(\hat{r})$ is the sum over two orthogonal polarizations of the maximum directivity radiated by the surface currents in direction $\hat{r}$. It should be noted that while the maximum directivity is mathematically infinite for any radiating surface, its practical limitation is based on neglecting radiation modes with small radiation resistance, which is the physical interpretation of (54). (We note that another way to limit the directivity is applying a finite local bandwidth [47] or imposing losses on the enveloping surface [48], [49], which is beyond the scope of this work.)

E. Reciprocity and Average Maximum Effective Area

The process described in Sections III-A and III-B is perfectly reciprocal. This means that we can assume incident plane waves from any directions and two orthogonal polarizations, and construct a matrix sampling the field on a box circumscribing the antenna. The sampling can be achieved by the use of electric and magnetic testing functions. By reciprocity, the obtained matrix will be identical to $\mathbf{F}$. Equation (56) assumes in this case the reciprocal form

$$A_{max}^{(ave)} = \frac{1}{\lambda^2}\int\int_{4\pi} A_{max}^{(\Sigma)}(\hat{r})d\Omega = \mathrm{trace}\left(\mathbf{F}^{\mathrm{H}}\mathbf{F}\right) \tag{57}$$

where $A_{max}^{(\Sigma)}$ is the sum of the effective areas associated with two orthogonally polarized waves with direction of incidence $-\hat{\mathbf{r}}$. Equation (57) can be obtained from (56) by using $D_{max}^{(\Sigma)} = A_{max}^{(\Sigma)}4\pi/\lambda^2$. We observe that in [25], the currents providing the maximum effective area are defined as canceling Huygens' source currents.

F. Quasi-Optical Closed-Form Approximation of the Trace

In Appendix C, it is shown that for a large dimension relative to the wavelength, and when the box thickness is negligible compared to the wavelength, (56) can be approximated as

$$D_{max}^{(ave)} = \mathrm{trace}\left(\mathbf{F}^{\mathrm{H}}\mathbf{F}\right) \approx \frac{2\pi A}{\lambda^2}. \tag{58}$$

This formula is obtained by assuming that no field is received when a plane wave is incident from the back of the array as suggested by Neto et al. [25]. It is also worth noting that when the dimension becomes very large, the eigenvalues of $\mathbf{F}^{\mathrm{H}}\mathbf{F}$ tend to equalize and exhibit a neat threshold behavior, beyond which they rapidly decay to zero [50]. Consequently, this implies

$$\mathrm{trace}\left(\mathbf{F}^{\mathrm{H}}\mathbf{F}\right) \to \mathrm{rank}_e\left(\mathbf{F}^{\mathrm{H}}\mathbf{F}\right) \quad \text{as} \quad \lambda^2/A \to 0 \tag{59}$$

indicating that (58) can also be interpreted as the asymptotic value for the optical regime of the DoFs for flat apertures. However, this asymptotic form is not a good approximation for typical dimensions of BTS, while (56) and its reciprocal version (57) are exact.

G. Complete Basis of Eigenfields

The first N_{DoF} columns of $\mathbf{v}$, namely,

$$\mathbf{v}_j \quad \text{for} \quad j = 1, \ldots, N_{DoF} \tag{60}$$

constitute a complete basis to represent the far field radiated in any region of space by any combination of currents on the box. Based on (50), this field can be represented as

$$\bar{\boldsymbol{E}}_j(\bar{r}) = \frac{e^{-jkr}}{r}\sqrt{P_j^{(rad)}}\,\bar{\boldsymbol{\chi}}_j(\hat{r}); \quad j = 1, \ldots, N_{DoF} \tag{61}$$

$$\bar{\boldsymbol{\chi}}_j(\hat{r}) = \sqrt{\zeta_0}\sum_{i=1}^{2}\sum_{n=1}^{N_b}\frac{1}{\sigma_j}\left(\bar{A}_n^{(i)}(\hat{\boldsymbol{r}})I_{n,j}^{(i)} + \bar{B}_n^{(i)}(\hat{\boldsymbol{r}})\tilde{I}_{n,j}^{(i)}\right) \tag{62}$$

where $I_{n,j}^{(i)}$ and $\tilde{I}_{n,j}^{(i)}$ are the dimensionless entries of the matrix $\mathbf{i}$ coming from the SVD in (50) and $P_j^{(rad)}$ is the associated radiated power. We note that the summation in (62) is truncated to the number of DoF in (54). The eigenfields $\bar{\boldsymbol{\chi}}_j(\hat{r})$ in (61) play the same role as the EEPs $\bar{\boldsymbol{\Phi}}_j(\hat{r})$ in (20); in contrast with $\bar{\boldsymbol{\Phi}}_j(\hat{r})$, they constitute a complete orthonormal basis for the description of *any* field radiated in the far zone from *any* currents inside the box. They can be thought of as associated with virtual ports that are perfectly matched, completely uncoupled from each other and without losses. Since the basis is complete, the use of these element patterns allows for establishing an upper bound for the correlation matrix of any finite antenna enclosed in the box. This is formalized in the next section with reference to a finite region of space in the far zone. We note that the completeness of the basis is only relevant to the far zone as formulated here; however, the process can be applied in the Fresnel zone as well. Furthermore, it can be extended to more complex scenarios by properly changing the Green's function.

VI. Upper Bounds and Figures of Merit

A. Correlation Matrix of the Eigenfields

We use here the complete set of eigenfields $\bar{\boldsymbol{\chi}}_j(\hat{r})$ found in the previous section for constructing a subset of eigenmodes representing a complete basis in a finite region of space. To this end, let us consider the CCM $N_{DoF} \times N_{DoF}$, associated with the far-field region Ω_c. We denote it as $\bar{\boldsymbol{\eta}}^{(c)}$. The entries of this matrix are

$$\bar{\eta}_{i,j}^{(c)} = \frac{1}{\zeta_0}\int\int_{\Omega_c}\bar{\boldsymbol{\chi}}_i^*(\hat{r})\cdot\bar{\boldsymbol{\chi}}_j(\hat{r})d\Omega. \tag{63}$$

The Hermitian correlation matrix $\bar{\boldsymbol{\eta}}^{(c)}$ can be diagonalized obtaining

$$\bar{\boldsymbol{\eta}}^{(c)} = \bar{Q}^{(\mathbf{c})}\bar{\Lambda}^{(\mathbf{c})}\bar{\boldsymbol{Q}}^{(c)\mathrm{H}} \tag{64}$$

where $\bar{Q}^{(\mathbf{c})}$ is a unitary matrix and $\bar{\Lambda}^{(\mathbf{c})}$ is a diagonal matrix with the real and positive eigenvalues $\bar{\lambda}_i$ of $\bar{\boldsymbol{\eta}}^{(c)}$ on the diagonal, arranged in a descending order. These eigenvalues represent the spill-over efficiencies of the eigenmodes since they are normalized by the radiated power and not by the incident power.

B. Upper Bound for the Number of MIMO Independent Channels

The DoF within the cell can be calculated by

$$N_{DoF}^{(c)} = \mathrm{rank}_e\left(\bar{\boldsymbol{\eta}}^{(c)}\right) \approx \mathrm{round}\left\{\frac{\left(\sum_i \bar{\lambda}_i^{(c)}\right)^2}{\sum_i\left(\bar{\lambda}_i^{(c)}\right)^2}\right\}. \tag{65}$$

We note that $\mathrm{trace}(\bar{\boldsymbol{\eta}}^{(c)}) < \mathrm{rank}_e(\bar{\boldsymbol{\eta}}^{(c)})$ since the eigenvalues of $\bar{\boldsymbol{\eta}}^{(c)}$ are all less than 1. Because of the completeness of $\bar{\boldsymbol{\chi}}_j(\hat{r})$, this number represents an upper bound to the number of independent MIMO channels

$$N_{MIMO} \le N_{DoF}^{(c)}. \tag{66}$$

C. Upper Bound of the Trace of the CCM

In a way similar to the one used for deriving (37) and (56), one finds

$$\frac{1}{4\pi}\int\int_{\Omega_c} D_{max}^{(\Sigma)}(\hat{r})d\Omega = \mathrm{trace}\left(\bar{\boldsymbol{\eta}}^{(c)}\right). \tag{67}$$

From the completeness of the basis used and for the fact that we have normalized the eigenmodes by the radiated power, while the EEP for the array is normalized by the input power, we also conclude that $\mathrm{trace}(\bar{\boldsymbol{\eta}}^{(c)})$ is the upper bound of $\mathrm{trace}(\boldsymbol{\eta}^{(c)})$; i.e., for any antenna contained in the box, one has

$$\mathrm{trace}\left(\boldsymbol{\eta}^{(c)}\right) \le \mathrm{trace}\left(\bar{\boldsymbol{\eta}}^{(c)}\right) \tag{68}$$

which, in terms of average maximum gain and directivity, reads

$$G_{max}^{(ave,c)} \le D_{max}^{(ave,c)} \tag{69}$$

where $D_{max}^{(ave,c)} = (1/\Omega_c)\int\int_{\Omega_c} D_{max}^{(\Sigma)}(\hat{r})d\Omega$ and $G_{max}^{(ave,c)}$ is defined in (37). In Appendix C, it is shown that for a large dimension relative to the wavelength, and when the box thickness is negligible compared to the wavelength, (37) can be approximated as

$$D_{max}^{(ave,c)} = \mathrm{trace}\left(\boldsymbol{\eta}^{(c)}\right) \approx \frac{2\pi A}{\lambda^2}\Omega_c' \quad \lambda^2/A \to 0 \tag{70}$$

where $\Omega_c' = \int\int_{\Omega_c}\hat{r}\cdot\hat{n}d\Omega$. We note that $A\Omega_c'$ can be seen as the projected area of the aperture normal to $\hat{r}$, averaged in the cell. This is in line with the "shadow area" concept in [51].

D. Antenna New Figures of Merit

Based on the bound in (66), (68), and (69), one can establish new figures of merit associated with the antenna and with the cell as follows:

Average Efficiency per Channel:

$$\eta_{ave} = \frac{\mathrm{trace}\left(\boldsymbol{\eta}^{(c)}\right)}{N_{MIMO}} = \frac{\mathrm{trace}\left(\boldsymbol{\eta}^{(c)}\right)}{\mathrm{rank}_e\left(\boldsymbol{\eta}^{(c)}\right)} \tag{71}$$

Average Maximum Gain Efficiency:

$$\eta_g = \frac{G_{max}^{(ave,c)}}{D_{max}^{(ave,c)}} = \frac{\mathrm{trace}\left(\boldsymbol{\eta}^{(c)}\right)}{\mathrm{trace}\left(\bar{\boldsymbol{\eta}}^{(c)}\right)} \tag{72}$$

Antenna Channel Effectiveness:

$$n_c = \frac{N_{MIMO}}{N_{DoF}^{(c)}} = \frac{\mathrm{rank}_e\left(\boldsymbol{\eta}^{(c)}\right)}{\mathrm{rank}_e\left(\bar{\boldsymbol{\eta}}^{(c)}\right)} \tag{73}$$

Antenna Port Effectiveness:

$$n_p = \frac{N_{MIMO}}{N} = \frac{\mathrm{rank}_e\left(\boldsymbol{\eta}^{(c)}\right)}{N}. \tag{74}$$

We note that all the parameters can be calculated by the eigenvalues of $\boldsymbol{\eta}^{(c)}$ and $\bar{\boldsymbol{\eta}}^{(c))}$. The parameter η_{ave} measures the ability of the antenna to create efficient orthogonal channels in the cell; the parameter η_g indicates how closely the antenna approaches the bound of average maximum gain; n_c compares the number of independent MIMO channels created by the antenna in the cell with respect to the upper bound of MIMO channels (the number of DoF). The parameter n_p reflects the level of redundant complexity in the system and tends to one when the number of ports matches the number of independent channels. These figures of merit are evaluated in the numerical results that follow.

VII. Numerical Results

In this section, we discuss a series of numerical results aimed at validating the theory outlined above. The results presented here, although relevant to simple examples, well represent practical problems that are of interest for base station antenna design. We will make reference to two antennas operating at 750 MHz, composed of 2×8 and 4×8 half-wavelength cross-dipoles, respectively, radiating with a finite ground plane [Fig. 5(a)]. The antennas are supposed to serve users arbitrarily distributed within a cell defined by $\theta \in [81°, 99°]$ and $\phi \in [-60°, 60°]$. The results are obtained using a commercial full-wave simulator (HFSS). Both arrays can be enclosed in a box $l_x = 0.2\lambda$, $l_y = 1.5\lambda$, and $l_z = 5\lambda$, where λ is the wavelength at 750 MHz, l_x is the distance of the dipoles from the ground plane, and $l_y \times l_z$ are the dimensions of the ground plane. We will refer to these two arrays as array A and array B.

1) *Array A:* Three configurations are considered.
   a) A: 64 ports. The array is considered with a number of ports equal to the number of dipoles.
   b) A1: 32 ports. The four columns in y are fed independently with different ports, while in the z-direction, the cross dipoles are grouped two by two, preserving the dual-polarization, and phasing the element to get the maximum at boresight.
   c) A2: 16 ports. Like in A1, but grouping elements along z in blocks of four, preserving the dual-polarization.
2) *Array B:* 32 ports. The array is considered with a number of ports equal to the number of dipoles.

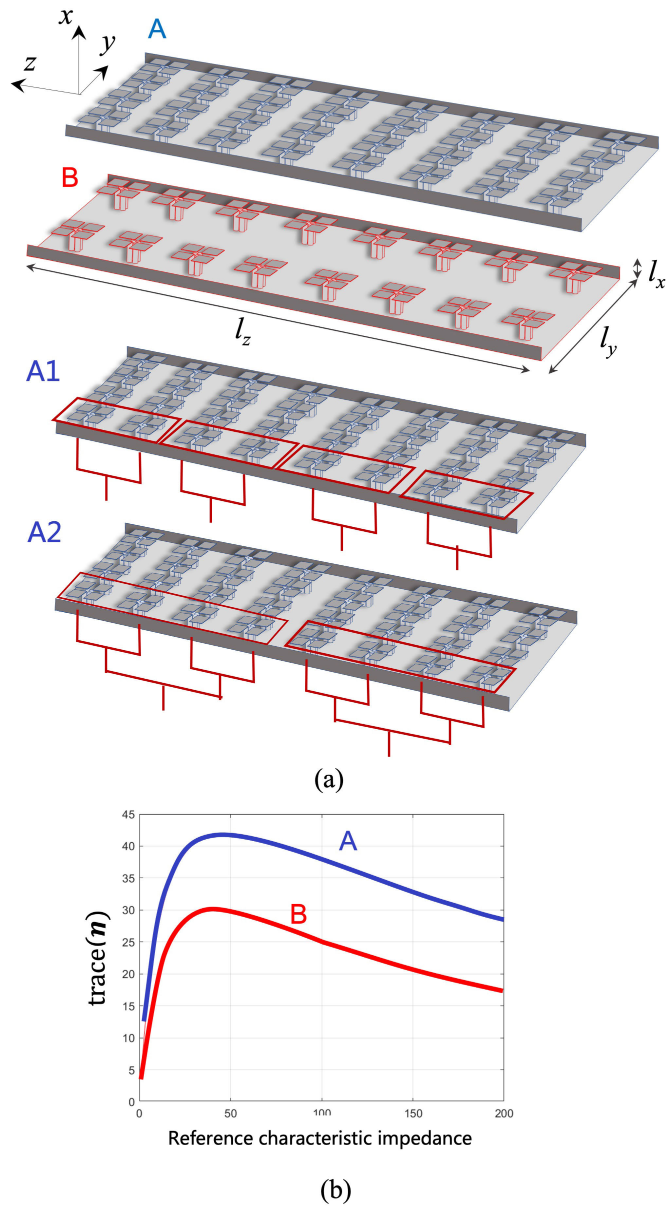

Fig. 5. (a) Different configurations of the antenna with interacting dipoles: array A (64 ports); array B (32 ports); array A1 (32 ports, obtained by grouping in couple ports of array A, preserving the dual-polarization); and array A2 (16 ports, obtained by grouping in quartet ports of array A, preserving the dual-polarization). (b) Trace of $\boldsymbol{\eta}$ as a function of the reference characteristic impedance of the transmission lines feeding the arrays A and B.

The origin of the reference system is set exactly at the center of the box enclosing the antenna. The centers of the dipoles are spaced by $5/8\lambda$ along z and $2/5\lambda$ along y for architecture A; $5/8\lambda$ along z and λ along y for architecture B.

For both architectures, the ports are fed with transmission lines of constant characteristic impedance. In order

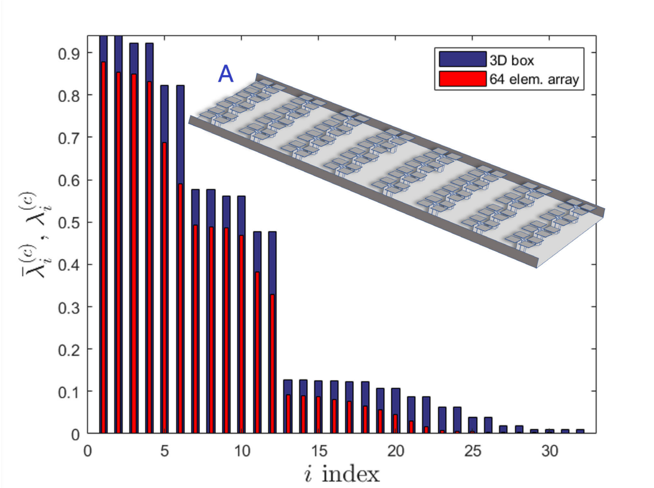

(a)

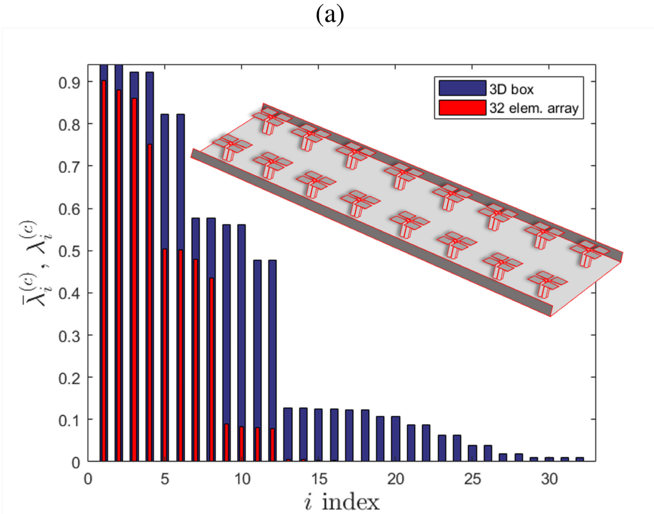

(b)

Fig. 6. Eigenvalues $\lambda_i^{(c)}$ of $\boldsymbol{\eta}^{(c)}$ (red bars) compared with the upper bound distribution of the eigenvalues $\bar{\lambda}_i^{(c)}$ of $\bar{\boldsymbol{\eta}}^{(c)}$ (blue bars). (a) Architecture A (64 ports). (b) Architecture B (32 ports).

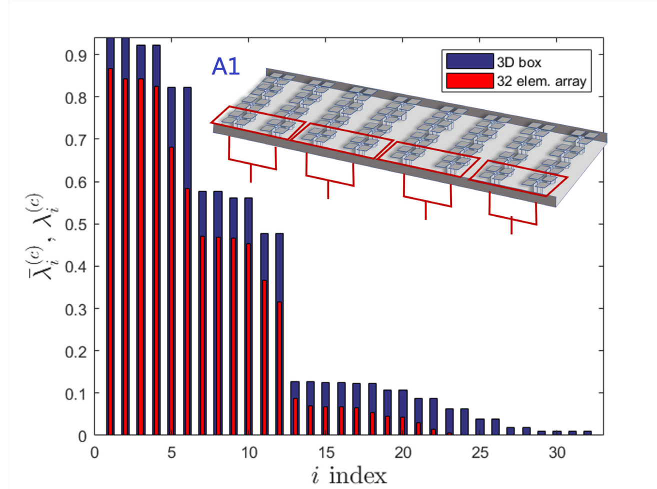

(a)

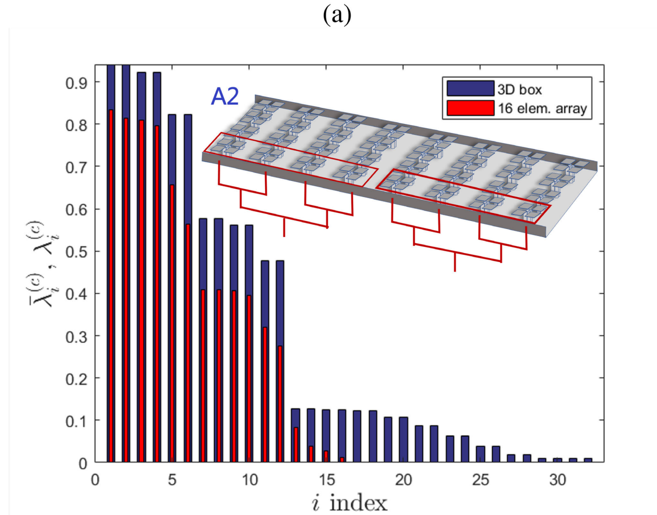

(b)

Fig. 7. Eigenvalues $\lambda_i^{(c)}$ of $\boldsymbol{\eta}^{(c)}$ (red bars) compared with the upper bound distribution of the eigenvalues $\bar{\lambda}_i^{(c)}$ of $\bar{\boldsymbol{\eta}}^{(c)}$ (blue bars). (a) Architecture A1 (32 ports). (b) Architecture A2 (16 ports).

to determine the best value for the latter, the impedance matrix at the ports, $\mathbf{Z}$, is exported, and $\boldsymbol{\eta} = \mathbf{1} - \mathbf{S}^{\mathrm{H}}\mathbf{S}$ is calculated, where

$$\mathbf{S} = (\mathbf{Z} - Z_0\mathbf{1})[\mathbf{Z} + Z_0\mathbf{1}]^{-1}.$$

Fig. 5(b) presents the trace of the ECM for the arrays A and B as a function of the characteristic impedance at the ports. It is observed that the trace of the ECM is close to its maximum value in both configurations for $Z_0 = 42\ \Omega$. Therefore, this value was chosen as the impedance of the transmission lines feeding the antenna elements. The distribution of eigenvalues of $\bar{\boldsymbol{\eta}}^{(c)}$ is represented by the blue bars in Figs. 6 and 7. Following the criterion established in (65), the DoF of the cell is $N_{DoF}^{(c)} = 16$ and $\mathrm{trace}(\bar{\boldsymbol{\eta}}^{(c)}) = 10.02$. (Note that the asymptotic approximation in (70) leads to $\mathrm{trace}(\bar{\boldsymbol{\eta}}^{(c)}) \approx 8.1$.) The average maximum directivity provided in (69) is given by $D_{max}^{(ave,c)} = 192$. These numbers represent the theoretical upper bounds for any array inside the box and are valid for the four cases A, B, A1, and A2.

The eigenvalues of $\eta^{(c)}$ are compared with the eigenvalues of $\bar{\boldsymbol{\eta}}^{(c)}$ in Fig. 6(a) and (b), respectively. The 64-port configuration (A) provides the following values:

$$13 = N_{MIMO} \leq N_{DoF}^{(c)} = 16 \tag{75}$$

$$8.1 = \mathrm{trace}\left(\boldsymbol{\eta}^{(c)}\right) \leq \mathrm{trace}\left(\bar{\boldsymbol{\eta}}^{(c)}\right) = 10.02 \tag{76}$$

$$155 = G_{max}^{(ave,c)} \leq D_{max}^{(ave,c)} = 192. \tag{77}$$

The 32-element configuration (B) provides instead

$$8 = N_{MIMO} \leq N_{DoF}^{cell} = 16 \tag{78}$$

$$5.66 = \mathrm{trace}\left(\boldsymbol{\eta}^{(c)}\right) \leq \mathrm{trace}\left(\bar{\boldsymbol{\eta}}^{(c)}\right) = 10.02 \tag{79}$$

$$109 = G_{max}^{(ave,c)} \leq D_{max}^{(ave,c)} = 192. \tag{80}$$

We analyze now the two configurations derived from the 64-port antenna array A by appropriately grouping its ports. Specifically, the two new configurations will have 32 (configuration A1) and 16 (configuration A2) ports, respectively. These configurations are obtained by grouping two and four consecutive blocks, respectively [Fig. 5(a)]. In grouping the

TABLE I
FIGURES OF MERIT OF THE VARIOUS ARRAY CONFIGURATIONS

Config.	N	n_c	η_g	η_{ave}	n_p
A	64	81%	81%	51%	20%
B	32	50%	56%	71%	25%
A1	32	81%	77%	60%	41%
A2	16	69%	68%	62%	69%

EEPs, each will be fed with an incident wave of constant amplitude equal to $1/\sqrt{2}$ and $1/2$, respectively, and phase such that maximum radiation is achieved at boresight. In doing that, it is assumed that a matching network at 42 Ω is realized. The eigenvalues of $\eta^{(c)}$ are compared with the eigenvalues of $\bar{\boldsymbol{\eta}}^{(c)}$ in Fig. 7(a) and (b), respectively. The analysis reveals the following values:

Architecture A1 (32 Ports):

$$13 = N_{MIMO} \leq N_{DoF}^{cell} = 16 \tag{81}$$

$$7.74 = \text{trace}\left(\boldsymbol{\eta}^{(c)}\right) \leq \text{trace}\left(\bar{\boldsymbol{\eta}}^{(c)}\right) = 10.02 \tag{82}$$

$$148 = G_{max}^{(ave,c)} \leq D_{max}^{(ave,c)} = 192. \tag{83}$$

Architecture A2 (16 Ports):

$$11 = N_{MIMO} \leq N_{DoF}^{cell} = 16 \tag{84}$$

$$6.85 = \text{trace}\left(\boldsymbol{\eta}^{(c)}\right) \leq \text{trace}\left(\bar{\boldsymbol{\eta}}^{(c)}\right) = 10.02 \tag{85}$$

$$131 = G_{max}^{(ave,c)} \leq D_{max}^{(ave,c)} = 192. \tag{86}$$

The figures of merit of the analyzed antenna configurations are summarized in Table I. From the analysis of these data, it can be seen for instance that configuration A1 and even A2 possess similar overall performance of configuration A, despite they have 1/2 and 1/4 the number of ports, respectively (namely, much higher n_p). Also, configuration B is definitely worse than A2, even if the latter has half of the number of ports.

VIII. CONCLUSION

We have investigated the interplay between the EEP and the ECM to model BTS array antenna performance in MIMO systems. The ECM predicts array antenna behavior and efficiency, with its link to the scattering matrix established under no-loss conditions, enabling correlation matrix estimation through simple port measurements.

Our investigation into maximum and average array efficiencies has shown their significant dependence on input coefficients. We have identified an orthogonal set of EEPs that optimize array performance, deriving expressions for average AE and maximum gain, which serve as benchmarks for practical antenna designs. Additionally, by analyzing the CCM and spill-over efficiency, we have maximized power within a defined cell, highlighting the importance of orthogonal field modes in enhancing MIMO channel effectiveness. We also presented a method to determine the effective number of independent MIMO channels.

The DoF of the EM field was quantified using currents on a minimal surface enclosing the array, linking these to orthonormal modal currents and fields. This analysis provided an upper bound on the number of independent MIMO channels, offering a theoretical limit for practical antenna designs.

Our findings emphasize the need for a comprehensive approach in antenna design, considering theoretical bounds and practical efficiencies. The complete basis of eigenfields can optimize the design process, ensuring maximal use of the available DoF. Numerical simulations have validated the theoretical models, providing a robust framework for designing future high-efficiency array antennas in MIMO systems and offering valuable insights for both theoretical exploration and practical design. Our methodologies pave the way for future research aimed at meeting the demands of high-performance wireless communication technologies.

For completeness, we report that during the review phase of this article, one of the reviewers brought to our attention a recent article by Gustafsson [51], published on ArXiv at the present state. The analysis in [51] demonstrates that the N_{DoF} for electrically large antennas and observation regions can be approximated by the mutual shadow area of the regions, measured in wavelengths for any type of object, whether convex or concave. This result valid at the optical limit of zero wavelength is in agreement with (58).

APPENDIX A
MAXIMUM AVERAGE EFFICIENCY FOR ANY POSSIBLE SETS OF ORTHOGONAL MODES

Let us consider a η matrix, which is hermitian and definite positive, and a matrix $\mathbf{A} = [\mathbf{a}_1, ..\mathbf{a}_N]$ that collects in its columns the vector of coefficient of the incident waves for a given set of excitations. Assume that $\mathbf{A}$ is as follows.

1) $\mathbf{A}$ is invertible.
2) $\mathbf{A}^{\mathrm{H}}\mathbf{A}$ has all 1 on the diagonal; this implies that the power associated with each excitation $\mathbf{a}_n$ is a unit power.
3) $\mathbf{A}^{\mathrm{H}}\boldsymbol{\eta}\mathbf{A} = \mathbf{D}$, being $\mathbf{D}$ diagonal. From (5), this implies that the radiated field associated with two different sets $\mathbf{a}_i$ and $\mathbf{a}_j$ are mutually orthogonal.

Note that the diagonal matrix $\mathbf{D}$ does not necessarily have on its diagonal the eigenvalues of $\boldsymbol{\eta}$ since the matrix $\mathbf{A}$ is not in general unitary. We would like now to demonstrate that

$$\text{trace}\{\mathbf{D}\} \leq \text{trace}(\boldsymbol{\eta}) = \sum_{i=1}^{N} \lambda_i \tag{87}$$

where the equality is obtained when $\mathbf{A}$ is a unitary matrix, namely, when the entries of $\mathbf{D}$ are the eigenvalues λ_i of $\boldsymbol{\eta}$. To this end, let us factorize $\mathbf{A}$ as $\mathbf{A} = \mathbf{QR}$, where $\mathbf{Q}$ is a unitary matrix and $\mathbf{R}$ is an upper triangular matrix. We note that all the elements of $\mathbf{R}$ have amplitude lower than or equal to 1 because $\mathbf{A}^{\mathrm{H}}\mathbf{A}$ has all 1 on the diagonal. We observe that the trace of $[\mathbf{A}^{\mathrm{H}}]^{-1}\mathbf{D}\mathbf{A}^{-1}$, which is equal to the trace of $[\mathbf{R}^{\mathrm{H}}]^{-1}\mathbf{D}\mathbf{R}^{-1}$, is greater than or equal to the trace of $\mathbf{D}$. It is also true that

$$\text{trace}\left\{\left[\mathbf{R}^{\mathrm{H}}\right]^{-1}\mathbf{D}\mathbf{R}^{-1}\right\} = ||\mathbf{D}^{\frac{1}{2}}\mathbf{R}^{-1}||^2 \geq ||\mathbf{D}^{\frac{1}{2}}||^2 = \text{trace}\{\mathbf{D}\} \tag{88}$$

where $||(\cdot)||$ indicates the Frobenius norm. The sequence in (88) is justified by the fact that the Frobenius norm of $\mathbf{D}^{(1/2)}\mathbf{R}^{-1}$ is greater than or equal to the

Frobenius norm of $\mathbf{D}^{(1/2)}$. The fact that $\mathbf{R}^{-1}$ is upper triangular and all the elements on its diagonal have amplitude greater than or equal to 1 implies that $\mathbf{D}^{0.5}\mathbf{R}^{-1}$ has on its diagonal the elements of $\mathbf{D}^{0.5}$ multiplied by a number whose amplitude is not lower than 1. As $\mathbf{D}^{(1/2)}$ has all 0 on the extra-diagonal terms, one concludes the validity of (87).

We can synthesize the above results as follows: among all the sets of orthogonal modes, the maximum average efficiency of the array is obtained when the wave coefficients at the ports are the normalized eigenvectors of the ECM.

Appendix B
Trace of ECM for a Regular Array

Let us consider a conventional periodic array with all elements corresponding to one port per polarization, with elements that are identical and positioned at the nodes of a regular periodic lattice covering a total aperture A. Let us denote with $a = d_x \times d_y$ the area of the single unit cell. The number of ports is, therefore, $N = 2A/a$, assuming that each element is associated with two ports, corresponding to orthogonal polarizations. Whenever $d_{x,y} < (\lambda/2)$, the array can scan the full space without grating lobes. However, coupling cannot be eliminated in such type of arrays [52], thus resulting in EEEs less than unity. It has been evidenced in [53] that the maximum possible EEE in the limit of identical radiation patterns (infinite array approximation) is $\pi a/\lambda^2$, thus producing $\mathrm{trace}(\boldsymbol{\eta}) = N\pi a/\lambda^2 = 2\pi A/\lambda^2$. Smaller spacing between adjacent elements rapidly increases the level of coupling, thus reducing the trace and the effective rank of $\boldsymbol{\eta}$. This is the reason why arranging dense elements into a constrained area, which leads to so-called holographic MIMO [54], [55], is affected by low efficiency [53], [56]. Conversely, increasing the spacing between adjacent elements reduces the impact of coupling, which, if the spacing is large enough, becomes negligible; however, when grating lobes emerge from grazing angles, a reduction of the EEE occurs due to input impedance mismatch.

Appendix C
Approximated Values of the Trace for Large Apertures

When the array is very thin and the aperture is large in terms of the wavelength, one may think that the box can be approximated by an aperture radiating only in the upper half space because of the presence of the ground plane. In such a case, denoted by A, the area of the aperture and $\hat{n}$ its normal directed toward the light region, the maximum directivity of the radiating aperture in direction $\hat{r}$ can be approximated as $D_{max}^{(\Sigma)}(\hat{r}) \approx \hat{r}\cdot\hat{n}4\pi A/\lambda^2(\hat{\theta}\cdot\hat{\theta}+\hat{\phi}\cdot\hat{\phi})$ for $\hat{r}\cdot\hat{n} \geq 0$ (light region) and zero for $\hat{r}\cdot\hat{n} \leq 0$ (shadow region). This approximation appears quite clear in reception since the aperture can at maximum entirely absorb the flux of any incident Poynting's vector coming from direction $-\hat{r}$ in the light region, and it is the same as that used in [25] and [51]. Furthermore, when the cell is in the light region, the average maximum directivity is given by $D_{max}^{(ave,c)} \approx 2A/\lambda^2 \int\int_{2\pi} \hat{r}\cdot\hat{n}d\Omega = 2\pi A/\lambda^2$ since the value of the integral is π that implies (58). This result is in agreement with the one discussed in Appendix B.

In case the integration is performed over a finite angle Ω_c in the light region, the above equation becomes $D_{max}^{(ave,c)} \approx 2A/\lambda^2 \int\int_{\Omega_c} \hat{r}\cdot\hat{n}d\Omega$, thus having $\mathrm{trace}(\boldsymbol{\eta}^{(c)}) \approx 2A/\lambda^2\Omega_c'$ where $\Omega_c' = \int\int_{\Omega_c} \hat{r}\cdot\hat{n}d\Omega$.

References

[1] *NR; User Equipment (UE) Radio Transmission and Reception; Part 1: Range 1 Standalone*, document TS 38.101-1, 3GPP, 2022.

[2] *User Equipment (UE) Radio Transmission and Reception*, document TS 36.101, 2022.

[3] Federal Communications Commission (FCC). (2022). *FCC Spectrum Allocation Chart*. [Online]. Available: https://www.fcc.gov/engineering-technology/policy-and-rules-division/radio-spectrum-allocation/general/table-frequency

[4] Global System for Mobile Communcation Association (GSMA). *GSMA Annual Report 2023*. [Online]. Available: https://www.gsma.com/about-us/wp-content/uploads/2024/06

[5] Next Generation Mobile Network (NGMN). (2022). *Recommendation on Base Station Active Antenna System, Standard V3*. [Online]. Available: https://www.ngmn.org/wp-content/uploads/230907_BASTA_AA_V3.0.pdf

[6] *NR; Base Station (BS) Radio Transmission and Reception*, document TS 38.104, 3GPP, 2022.

[7] *Study on Channel Model for Frequencies From 0.5 To 100 Ghz*, document TR 38.901, v18.0.0, 3GPP, 2022.

[8] F. Rusek et al., "Scaling up MIMO: Opportunities and challenges with very large arrays," *IEEE Signal Process. Mag.*, vol. 30, no. 1, pp. 40–60, Jan. 2013.

[9] E. G. Larsson, O. Edfors, F. Tufvesson, and T. L. Marzetta, "Massive MIMO for next generation wireless systems," *IEEE Commun. Mag.*, vol. 52, no. 2, pp. 186–195, Feb. 2014.

[10] C. Craeye and D. González-Ovejero, "A review on array mutual coupling analysis," *Radio Sci.*, vol. 46, no. 2, pp. 1–25, Apr. 2011.

[11] X. Chen et al., "Revisit to mutual coupling effects on multi-antenna systems," *J. Commun. Inf. Netw.*, vol. 5, no. 4, pp. 411–422, Dec. 2020.

[12] X. Gao, L. Dai, Y. Wang, and L. Hanzo, "Transmit optimization for multi-antenna NOMA systems," *IEEE Trans. Commun.*, vol. 63, no. 12, pp. 4675–4690, 2015.

[13] H. Zhang, H. Dai, and C.-X. Wang, "Survey of enabling technologies for 5G networks: Phy layer and radio access network perspectives," *IEEE Access*, vol. 7, pp. 77572–77595, 2019.

[14] E. Björnson, J. Hoydis, and L. Sanguinetti, "Massive MIMO networks: Spectral, energy, and hardware efficiency," 2017, doi: 10.1561/2000000093.

[15] A. Gupta and R. K. Jha, "A survey of 5G network: Architecture and emerging technologies," *IEEE Access*, vol. 3, pp. 1206–1232, 2015, doi: 10.1109/ACCESS.2015.2461602.

[16] H. Huh, G. Caire, H. C. Papadopoulos, and S. A. Ramprashad, "Achieving 'Massive MIMO' spectral efficiency with a not-so-large number of antennas," *IEEE Trans. Wireless Commun.*, vol. 11, no. 9, pp. 3226–3239, Sep. 2012.

[17] H. Q. Ngo, E. G. Larsson, and T. L. Marzetta, "Energy and spectral efficiency of very large multiuser MIMO systems," *IEEE Trans. Commun.*, vol. 61, no. 4, pp. 1436–1449, Apr. 2013.

[18] T. S. Rappaport et al., "Millimeter wave mobile communications for 5G cellular: It will work!" *IEEE Access*, vol. 1, pp. 335–349, 2013.

[19] J. G. Andrews et al., "What will 5G be?" *IEEE J. Sel. Areas Commun.*, vol. 32, no. 6, pp. 1065–1082, Jun. 2014.

[20] R. W. Heath, A. Paulraj, and J. Balakrishnan, "Diversity in wireless communications: Concepts and technologies," *IEEE Trans. Veh. Technol.*, vol. 53, no. 6, pp. 962–968, Jun. 2005, doi: 10.1109/TCOMM.2005.849774.

[21] S. Ahmadi, *5G NR: Architecture, Technology, Implementation, and Operation of 3GPP New Radio Standards*. New York, NY, USA: Academic, Jun. 2019.

[22] Q. C. Li, H. Niu, A. T. Papathanassiou, and G. Wu, "5G network capacity: Key elements and technologies," *IEEE Vehicular Technol. Mag.*, vol. 9, no. 1, pp. 71–78, Mar. 2014, doi: 10.1109/MVT.2013.2295070.

[23] M. Di Renzo and S. Tretyakov, "Reconfigurable intelligent surfaces [scanning the issue]," *Proc. IEEE*, vol. 110, no. 9, pp. 1159–1163, Sep. 2022.

[24] E. Martini and S. Maci, "Theory, analysis, and design of metasurfaces for smart radio environments," *Proc. IEEE*, vol. 110, no. 9, pp. 1227–1243, Sep. 2022.

[25] A. Neto, N. Llombart, and A. Freni, "The observable field for antennas in reception," *IEEE Trans. Antennas Propag.*, vol. 66, no. 4, pp. 1736–1746, Apr. 2018.

[26] A. Neto, A. F. Bernardis, D. Emer, A. Freni, and N. Llombart, "The observable field in complex scattering scenarios," *IEEE Trans. Antennas Propag.*, vol. 68, no. 7, pp. 5544–5555, Jul. 2020.

[27] R. Ozzola, D. Cavallo, A. Freni, N. Llombart, and A. Neto, "A benchmark for the number of independent line of sight links on a given volume platform," *IEEE Trans. Antennas Propag.*, vol. 70, no. 12, pp. 12071–12080, Dec. 2022.

[28] O. M. Bucci and G. Franceschetti, "On the degrees of freedom of scattered fields," *IEEE Trans. Antennas Propag.*, vol. 37, no. 7, pp. 918–926, Jul. 1989.

[29] M. Franceschetti, M. D. Migliore, and P. Minero, "The capacity of wireless networks: Information-theoretic and physical limits," *IEEE Trans. Inf. Theory*, vol. 55, no. 8, pp. 3413–3424, Aug. 2009.

[30] M. D. Migliore, "On the role of the number of degrees of freedom of the field in MIMO channels," *IEEE Trans. Antennas Propag.*, vol. 54, no. 2, pp. 620–628, Feb. 2006.

[31] M. D. Migliore, "On electromagnetics and information theory," *IEEE Trans. Antennas Propag.*, vol. 56, no. 10, pp. 3188–3200, Oct. 2008.

[32] M. D. Migliore, "Horse (electromagnetics) is more important than horseman (information) for wireless transmission," *IEEE Trans. Antennas Propag.*, vol. 67, no. 4, pp. 2046–2055, Apr. 2019.

[33] R. Somaraju and J. Trumpf, "Degrees of freedom of a communication channel: Using DOF singular values," *IEEE Trans. Inf. Theory*, vol. 56, no. 4, pp. 1560–1573, Apr. 2010.

[34] R. Harrington and J. Mautz, "Theory of characteristic modes for conducting bodies," *IEEE Trans. Antennas Propag.*, vol. AP-19, no. 5, pp. 622–628, Sep. 1971.

[35] M. Gustafsson, L. Jelinek, K. Schab, and M. Capek, "Unified theory of characteristic modes—Part I: Fundamentals," *IEEE Trans. Antennas Propag.*, vol. 70, no. 12, pp. 11801–11813, Dec. 2022.

[36] C. Ehrenborg, M. Gustafsson, and M. Capek, "Capacity bounds and degrees of freedom for MIMO antennas constrained by Q-factor," *IEEE Trans. Antennas Propag.*, vol. 69, no. 9, pp. 5388–5400, Sep. 2021.

[37] M. Capek and L. Jelinek, "Transducer and radiation efficiency figures of a multiport antenna array," *IEEE Trans. Antennas Propag.*, vol. 71, no. 7, pp. 6132–6137, Jul. 2023.

[38] V. Neuman, M. Capek, L. Jelinek, A. Lehtovuori, and V. Viikari, "Trade-off between optimal efficiency and envelope correlation coefficient of MIMO antenna clusters," *IEEE Trans. Antennas Propag.*, vol. 72, no. 6, pp. 4785–4795, Jun. 2024.

[39] S. Mikki, "The Shannon information capacity of an arbitrary radiating surface: An electromagnetic approach," *IEEE Trans. Antennas Propag.*, vol. 71, no. 3, pp. 2556–2570, Mar. 2023.

[40] S. Stein, "On cross coupling in multiple-beam antennas," *IRE Trans. Antennas Propag.*, vol. 10, no. 5, pp. 548–557, Sep. 1962.

[41] S. Blanch, J. Romeu, and I. Corbella, "Exact representation of antenna system diversity performance from input parameter description," *Electron. Lett.*, vol. 39, no. 9, pp. 705–707, May 2003.

[42] E. E. Altshuler, T. H. O'Donnell, A. D. Yaghjian, and S. R. Best, "A monopole superdirective array," *IEEE Trans. Antennas Propag.*, vol. 53, no. 8, pp. 2653–2661, Aug. 2005.

[43] D. S. Shiu, G. J. Foschini, M. J. Gans, and J. M. Kahn, "Fading correlation and its effect on the capacity of multielement antenna systems," *IEEE Trans. Commun.*, vol. 48, no. 3, pp. 502–513, Mar. 2000.

[44] S. S. A. Yuan, Z. He, X. Chen, C. Huang, and W. E. I. Sha, "Electromagnetic effective degree of freedom of an MIMO system in free space," *IEEE Antennas Wireless Propag. Lett.*, vol. 21, no. 3, pp. 446–450, Mar. 2022.

[45] P.-S. Kildal, E. Martini, and S. Maci, "Degrees of freedom and maximum directivity of antennas: A bound on maximum directivity of nonsuperreactive antennas," *IEEE Antennas Propag. Mag.*, vol. 59, no. 4, pp. 16–25, Aug. 2017.

[46] J. L. A. Quijano and G. Vecchi, "Improved-accuracy source reconstruction on arbitrary 3-D surfaces," *IEEE Antennas Wireless Propag. Lett.*, vol. 8, pp. 1046–1049, 2009.

[47] L. Passalacqua, C. Yepes, E. Martini, and S. Maci, "Q-bounded maximum directivity of self-resonant antennas," *IEEE Trans. Antennas Propag.*, vol. 71, no. 12, pp. 9549–9558, Dec. 2023.

[48] L. Passalacqua, C. Yepes, A. M. Barrera, B. Biscontini, E. Martini, and S. Maci, "Maximum gain of lossy antennas without and with Q-bounds," *IEEE Trans. Antennas Propag.*, vol. 72, no. 4, pp. 3033–3043, Apr. 2024.

[49] M. Gustafsson and M. Capek, "Maximum gain, effective area, and directivity," *IEEE Trans. Antennas Propag.*, vol. 67, no. 8, pp. 5282–5293, Aug. 2019.

[50] O. M. Bucci, "Computational complexity in the solution of large antenna and scattering problems," *Radio Sci.*, vol. 40, no. 6, pp. 1–9, Dec. 2005.

[51] M. Gustafsson, "Shadow area and degrees of freedom for free-space communication," 2024, *arXiv:2407.21122*.

[52] P. Hannan, "The element-gain paradox for a phased-array antenna," *IEEE Trans. Antennas Propag.*, vol. AP-12, no. 4, pp. 423–433, Jul. 1964.

[53] P.-S. Kildal, A. Vosoogh, and S. Maci, "Fundamental directivity limitations of dense array antennas: A numerical study using Hannan's embedded element efficiency," *IEEE Antennas Wireless Propag. Lett.*, vol. 15, pp. 766–769, 2016.

[54] L. Wei et al., "Multi-user holographic MIMO surfaces: Channel modeling and spectral efficiency analysis," *IEEE J. Sel. Topics Signal Process.*, vol. 16, no. 5, pp. 1112–1124, Aug. 2022.

[55] C. Huang et al., "Holographic MIMO surfaces for 6G wireless networks: Opportunities, challenges, and trends," *IEEE Wireless Commun.*, vol. 27, no. 5, pp. 118–125, Oct. 2020.

[56] S. S. A. Yuan, X. Chen, C. Huang, and W. E. I. Sha, "Effects of mutual coupling on degree of freedom and antenna efficiency in holographic MIMO communications," *IEEE Open J. Antennas Propag.*, vol. 4, pp. 237–244, 2023.

Federico Puggelli (Member, IEEE) was born in Prato, Italy, in 1978. He received the Laurea degree in telecommunications engineering from the University of Florence, Florence, Italy, and the Ph.D. degree in information engineering from the University of Siena, Siena, Italy, in 2007 and 2012, respectively.

Since 2012, he has been collaborating with the ElectroScience Laboratory, Department of Electrical and Computer Engineering, The Ohio State University, Columbus, OH, USA, where he was an Invited Visiting Scholar from March to September 2012, under the supervision of Prof. P. H. Pathak. Since 2018, he has been collaborating with PNRA (Italian Antarctic Research Program). He took part in the XXXIVth and XXXVth Italian expeditions to the Antarctic continent (austral summer 2018–2019 and 2019–2020, respectively). Since 2020, he has been with Huawei, first as a consultant for Huawei Deutschland, Munich, Germany, and then as an employee for Huawei Technologies S.r.l., Milan, Italy. His research interests include high-frequency techniques, the modeling of fading channels, and the dielectric characterization of the Antarctic ice sheet in the microwave range, along with topics related to information electromagnetics, such as the characterization of base station antennas within the cellular network.

Bruno Biscontini (Member, IEEE) was born in Gualdo Tadino, Italy, in 1976. He received the Laurea degree in electrical engineering from the University of Perugia, Perugia, Italy, in 2001, and the Ph.D. degree (Hons.) from the Technical University of Munich (TUM), Munich, Germany.

From 2002 to 2006, he was a Research Scientist and an Assistant Professor with TUM, following several research paths on electromagnetic field theory, antennas, and grid computing applied to electromagnetics. Since 2011, he has been the Director of RF system engineering and the Chief AAS Architect with the German Research Center, Huawei Technologies, Munich. He was also elected as the Chairperson of the Next Generation Mobile Communications Networks BASTA Active Antenna Group, NGMN Alliance, Frankfurt, Germany. He has authored or co-authored more than 25 publications in conferences, journals, and books, and holds more than 73 patents.

Dr. Biscontini was awarded the Dr. Spinner Price by TUM for his Ph.D. thesis and the Young Scientist by IEEE for his work on grid computing for electromagnetics.

Enrica Martini (Senior Member, IEEE) was born in Spilimbergo, Italy, in 1973. She received the Laurea degree (cum laude) in telecommunication engineering from the University of Florence, Florence, Italy, in 1998, and the joint Ph.D. degree in informatics and telecommunications and electronics from the University of Florence and the University of Nice-Sophia Antipolis, Nice, France, in 2002.

From 1998 to 1999, she was with the University of Florence, under a research grant from Alenia Aerospazio, Rome. In 2002, she became a Research Associate with the University of Siena, Siena, Italy. In 2005, she received the Hans Christian Ørsted Post-Doctoral Fellowship from the Technical University of Denmark, Lyngby, Denmark, where she worked with the Electromagnetic Systems Section until 2007. From 2007 to 2017, she was a Post-Doctoral Fellow with the University of Siena. In 2012, she co-founded the start-up Wave Up Srl, Siena, where she served as the CEO from 2016 to 2018. From 2019 to 2021, she was an Assistant Professor with the University of Siena, where she is currently an Associate Professor with the Department of Information Engineering and Mathematics. She has coordinated research projects funded by national and international institutions and industries. Her research interests include metasurfaces, metamaterial characterization, metasurface-based antennas and microwave devices, electromagnetic scattering, antenna measurements, and tropospheric propagation.

Dr. Martini co-received the 2016 Schelkunoff Transactions Prize Paper Award, the Best Paper Award in Antenna Design and Applications at EuCAP 2017, the Best Poster Award at the Metamaterials Congress 2019, and the Best Paper Award in Electromagnetics at EuCAP 2021.

Stefano Maci (Fellow, IEEE) has been a Professor with the University of Siena, Siena, Italy, since 1997, leading a research group of 15 scholars. From 2004 to 2007, he was a Leader with the Antenna Center of Excellence (ACE, FP6-EU). In 2004, he founded the European School of Antennas (ESoA), which offers 34 postgraduate courses in antennas, propagation, electromagnetic theory, and computational electromagnetics. From 2007 to 2010, he coordinated a 24-institution Marie Curie Action (FP6). From 2008 to 2015, he directed the Ph.D. Program in information engineering and mathematics, coordinating 60 Ph.D. students annually. With more than 150 teachers from 15 countries, he has served as the ESoA Director since its inception. He has authored more than 200 journal articles, 14 book chapters, and 600 conference papers. His research spans high-frequency and beam representation methods, computational electromagnetics, phased arrays, planar and reflector antennas, metamaterials, and metasurfaces.

Dr. Maci has held leadership roles in professional organizations, including served on the IEEE Antennas and Propagation Society (AP-S) AdCom from 2012 to 2014, as an Associate Editor for IEEE TRANSACTIONS ON ANTENNAS AND PROPAGATION, and on the Board of Directors of the European Association on Antennas and Propagation (EurAAP). He was the President of IEEE AP-S in 2023 and is currently the Chair of the IEEE AP-S Field Award Committee. He has been a principal investigator of multiple projects, founding and directing the FORESEEN Consortium with 48 European institutions, from 2014 to 2018. He also led the "Nanoarchitectronics" Future Emerging Technology Project (EU Framework 8) and the EU Program "Metamask." Since 2010, he has been coordinating over 50 projects, including 15 for the European Space Agency, and co-founded two spin-off companies. Recognized globally as an educator and a researcher, he has been a Distinguished Lecturer of IEEE AP-S and EurAAP. He was a recipient of the EurAAP Award in 2014, IEEE Schelkunoff Prize in 2016, Chen-To Tai Educator Award in 2016, URSI Dellinger Medal in 2020, and the Italian Knowledge Leader Award in 2024. Over two decades, he has served on technical advisory boards for 20 international conferences and review boards for six journals. In the last decade, he delivered 60 keynote addresses or distinguished lectures and was the Technical Program Chair of METAMATERIAL 2020 and the General Chair of EuCAP 2023.